PERGAMON

International Journal of Heat and Mass Transfer 44 (2001) 4287–4311

International Journal of HEAT and MASS TRANSFER

www.elsevier.com/locate/ijhmt

Pool-boiling CHF enhancement by modulated porous-layer coating: theory and experiment

Scott G. Liter, Massoud Kaviany *

2250 G.G. Brown Laboratory, Department of Mechanical Engineering and Applied Mechanics, University of Michigan, 2350 Hayward Avenue, Ann Arbor, MI 48109-2125, USA

Received 3 July 2000; received in revised form 12 January 2001

Abstract

Modulated (periodically non-uniform thickness) porous-layer coatings, as an example of capillary artery-evaporator systems, are experimentally shown to enhance the pool-boiling critical heat flux nearly three times over that of a plain surface. The modulation separates the liquid and vapor phases, thus reducing the liquid–vapor counterflow resistance adjacent to the surface. Theories are suggested for two independent mechanisms capable of causing the liquid choking that leads to the critical heat flux. The Zuber hydrodynamic theory is modified to account for the effect of the coating modulation-wavelength on the development of the stable vapor layer above the coated surface, which effectively chokes the liquid down-flow towards the surface (above the coating). The second liquid-choking limit occurs within the porous-layer coating when the viscous drag surpasses the available capillary pumping. The lower of these liquid-choking limits, for a given set of geometrical and thermophysical parameters, is theorized to predict the observed critical heat flux. The predicted wetted-surface regime and the two limits are compared with the experimental results and good agreement is found. The theories are then used to discuss the optimization of the enhancement and suggest that completely separated liquid and vapor flow paths can result in substantial further enhancement.

1. Introduction

The efficiency and performance of devices experiencing high heat loads is often limited by the relationship between the generation or storage of heat in the device and the associated elevated and often undesirable device material temperatures. Examples of such limitations can be found in electronic cooling [1,2], the increasing of the efficiency of process and heat transfer equipment, among others [3–5]. Future technologies promise ever higher heat loads and compel the search for improved heat transfer (removal) systems.

Nucleate pool boiling is a well-recognized means for passively removing high heat loads from a device while maintaining relatively low material temperatures. Various surface modifications, including integrated surface structures (e.g., channels and fins) and the application of a uniform thickness porous-layer coating to the surface, have been shown to passively provide effective enhancement to boiling heat transfer [4,5]. Fig. 1 presents a map of the potential enhancement of surface modifications as collected from the published experimental data. Thin uniform thickness porous-layer coating of boiling surfaces has been experimentally proven to be an especially effective passive enhancement technique capable of providing an increase in the critical heat flux q_{CHF}, and/or a reduction in the surface superheat, $T_s - T_{lg}$, for a given surface heat flux q, compared to the performance of a plain surface [6–13]. A number of phenomenological theories have been put forth to explain boiling heat transfer from porous-layer coatings. The enhancement is attributed to combinations of an extended surface area effect, a capillary-assist to liquid flow effect, an increased nucleation site density effect, and the dependence of the vapor escape paths from the porous-layer on the pore

* Corresponding author. Tel.: +1-734-764-2694; fax: +1-734-647-3170.

E-mail addresses: liter@engin.umich.edu (S.G. Liter), kaviany@umich.edu (M. Kaviany).

0017-9310/01/$ - see front matter
PII: S0017-9310(01)00084-9

Nomenclature

a	area ratio
A	area $(\mathrm{m})^2$
c_p	specific heat (J/kg K)
Ca	capillary number, see Eq. (19)
C_E	Ergun coefficient
d	diameter (m)
Δh_lg	enthalpy of vaporization (J/kg)
g	gravitational acceleration $(\mathrm{m/s}^2)$
h	enthalpy (J/kg)
H	capillary rise height (m)
i	axial node counter
j	radial node counter
J	Leverett J-function, $J = J(s)$
Ja	Jakob number, $Ja = c_{\mathrm{p,l}}(T_\mathrm{s} - T_\mathrm{lg})/\Delta h_\mathrm{lg}$
k	thermal conductivity (W/m K)
K	absolute permeability tensor (m^2)
ℓ	thermal diffusion thickness (m)
M	molecular weight (kg/kmol)
N	size of computational domain $(N \times N)$
p	pressure (Pa)
Pe	Peclet number, $Pe_\mathrm{d} = \langle u_\mathrm{l}\rangle d/\alpha_\mathrm{l}$
q	heat flux $(\mathrm{W/m}^2)$
Q	heat transfer rate (W)
r	spatial coordinate, or radius (m)
R	base radius (m), or radius of curvature (m), or universal gas constant (J/kmol K)
Re_d	Reynolds number, see Eq. (14)
s	saturation
T	temperature (K)
u	velocity, or axial velocity (m/s)
v	radial velocity (m/s)
$We_{K^{1/2}}$	Weber number, see Eq. (19)
x	spatial coordinate, or height (m)
Z	Melrose function, $Z = Z(\theta_\mathrm{c})$

Greek symbols

δ	coating thickness (m)
ϵ	porosity, or area fraction
λ	flow-critical length scale (m), or wavelength (m)
μ	dynamic viscosity (kg/m s)
ρ	density $(\mathrm{kg/m}^3)$
σ	surface tension (N/m)
θ	included cone angle (degrees)
θ_c	contact angle (degrees)

Subscripts

b	base layer, or base of characteristic hydrodynamic cell
c	most critical λ_RT, or curvature, or capillary
CHF	critical heat flux
d	diameter, or most dangerous λ_RT
f	flow corridor
g	gas (vapor), gas flow
h	hydrodynamic limit
i	axial node counter
j	radial node counter
$j_{e,i}$	last node of row i, $j_{e,i} = N - i + 1$
$j_{o,i}$	first node of flow corridor in row i, $j_{o,i} = i_\mathrm{s} - i + 1$
J	Leverett coefficient, $C_J = 0.53$
k	conduction
ku	conduction–convection
KH	Kelvin–Helmholtz
l	liquid
lg	liquid–vapor, or saturation
m	modulation
p	plain (i.e., uncoated)
R	Rayleigh, or critical radius coefficient
r	radial direction
RT	Rayleigh–Taylor
s	solid, surface, or stack
u	uniform porous-layer coating
v	viscous-drag limit
Z	Zuber correlation for q_CHF
θ	included cone angle

Superscript

d	dispersion

Symbols

$*$	non-dimensionalized
$\langle\ \rangle$	volume or space averaged
$\parallel, \perp$	parallel and perpendicular to fluid flow

distribution at the top of the layer adjacent to the liquid pool. These effects are dependent on the fluid and solid thermophysical properties and geometrical coating parameters, such as coating thickness δ and pore size distribution. The exact relational dependence is not well understood and the extent of possible enhancement is not known. Due to the complexity of the flow conditions and phase-change processes inside and near the porous coating, analytical models have not been developed that have proven to be applicable over a wide range of the physical parameters without the use of the several empirical constants.

In a general sense, the limit on the q_CHF of any evaporating (e.g., pool boiling) system depends on the mechanisms of liquid supply to and vapor escape from the phase-change interface, and therefore can be considered to be limited by the liquid and vapor flow resistances. The theoretical maximum would then be the kinetic limit for the resistance to the evaporated vapor molecules leaving the liquid–vapor interface, or that

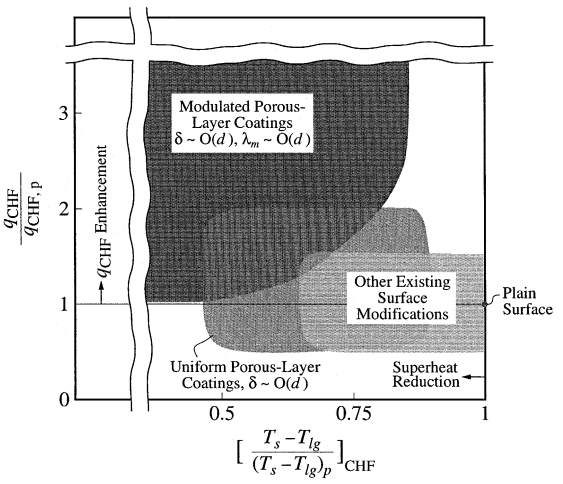

Fig. 1. The potential of various surface modifications used to enhance pool boiling.

described by Gambill and Lienhard [14] as the kinetic limit for evaporation given by

$$\frac{q_{\mathrm{CHF,max}}}{\left(R_{\mathrm{g}}/2\pi M\right)^{1/2}\Delta h_{\mathrm{lg}}(p_{\mathrm{g}})\left[\rho_{\mathrm{g}}(p_{\mathrm{g}})T_{\mathrm{lg}}^{1/2}(p_{\mathrm{g}})-\rho_{\mathrm{g},\infty}T_{\mathrm{lg},\infty}^{1/2}\right]}=1, \tag{1}$$

where $\rho_{\mathrm{g}}, T_{\mathrm{lg}}$, and Δh_{lg} are functions of the local vapor pressure, p_{g}, at the liquid–vapor interface, and where subscript "∞" denotes a far-field pressure assumed here to be $p_{\mathrm{g},\infty}=1$ atm. The interface p_{g} is higher than the far-field pressure due to the flow of evaporated molecules leaving the interface resulting from the evaporation. As an example, Eq. (1) results in $q_{\mathrm{CHF,max}}=8.09\times10^{7}\ \mathrm{W/m^2}$ for pentane, at $p_{\mathrm{g}}=1$ atm, evaporating to a vacuum, $p_{\mathrm{g},\infty}=0$. In practice, achievable, passively enhanced and sustainable q_{CHF} are smaller by two orders of magnitude. But this shows that there is much room for enhancement.

Within the liquid pool above the surface, and to a certain extent within porous layers of uniform layer thickness, the liquid supply and vapor escape occur as a liquid–vapor counterflow resisting each others motion. As the heat flux is increased, the liquid flow rate supplying the resulting evaporation, and in turn the liquid flow resistance, must increase. Eventually, a q_{CHF} is reached where either the liquid flow towards the phase-change interface chokes as in the case for high effusivity surfaces (i.e., high $\ell(\rho c_{\mathrm{p}}k)_{\mathrm{s}}^{1/2}$ surface and coating materials capable of maintaining a nearly uniform temperature), or the phase-change interface is reduced due to the development of local material hot spots above a critical rewetting temperature (local dryout locations) as in the case for low effusivity surfaces. This work restricts itself to cases where the surface and coating materials are assumed to exhibit high effusivity.

In pool boiling from high effusivity plain (uncoated) surfaces, the resistance to liquid flow towards the surface can be considered to arise from the thermal-hydraulics in the liquid–vapor counterflow directly above the surface and in the liquid pool. Zuber [15] theorized for infinite plain surfaces that the hydrodynamics impose stability limits to the counterflow determining a hydrodynamic liquid-choking limit (i.e., critical heat flux $q_{\mathrm{CHF,Z}}=q_{\mathrm{CHF,p}}$, where subscript "Z" denotes the Zuber hydrodynamic limit, and where subscript "p" denotes a plain surface).

In boiling from thick porous layers, there is an additional resistance to the liquid–vapor counterflow imposed by the solid porous matrix that can act to "trap" the escaping vapor above the phase-change interface and within the layer, thus reducing the relative permeability of the liquid and causing a viscous-drag determined dryout at fluxes much lower than that of plain surfaces (i.e., $q_{\mathrm{CHF,v}}\leq q_{\mathrm{CHF,p}}$, where subscript "v" denotes the viscous-drag liquid-choking limit) [16,17]. Udell [17] derived an expression for the critical heat flux of a deep porous layer with internal liquid–vapor counterflow, $q_{\mathrm{CHF,cf}}=q_{\mathrm{CHF,v}}|_{\delta\to0}$, as

$$\frac{q_{\mathrm{CHF,cf}}}{K\rho_{\mathrm{g}}\Delta h_{\mathrm{lg}}g(\rho_{\mathrm{l}}-\rho_{\mathrm{g}})/\mu_{\mathrm{g}}\left[1+\left(\rho_{\mathrm{l}}\mu_{\mathrm{g}}/\rho_{\mathrm{g}}\mu_{\mathrm{l}}\right)^{1/4}\right]^{-4}}=1. \tag{2}$$

Thin porous layers, however, when not thick enough to appreciably resist vapor escape, have been shown to enhance the critical heat flux (i.e., $q_{\mathrm{CHF,v}}\geqslant q_{\mathrm{CHF,p}}$) [8–11,18]. This enhancement is believed to be due to the lateral capillary-assist to the liquid-flow towards the phase-change interface, which reduces the liquid–vapor counter flow resistance (i.e., provides perferential flow paths for the liquid and vapor, or phase separation) and hinders the development of localized dryout conditions. The porous layer also creates non-hydrodynamically determined locations of vapor escape into the liquid pool possibly altering the thermal-hydraulics and extending the hydrodynamic liquid-choking limit (i.e., $q_{\mathrm{CHF,h}}>q_{\mathrm{CHF,Z}}$) [12,18].

The use of porous layer coating to enhance the evaporation rate (i.e., q_{CHF}) is an example of a more general class of thermal systems utilizing a liquid-supply artery to feed an evaporation zone. The capillary pumping in the porous media generates the required liquid draw thus establishing the fluid flow artery. By designing the artery to provide controlled direction to the liquid and vapor flows, and to minimize the liquid–vapor counterflow resistance (i.e., create phase separation with directed flow paths), significant enhancement in the sustainable heat loads can be achieved.

This work endeavors to theoretically analyze and experimentally utilize such an artery-evaporator system. Specifically, the advantages of porous-layer coatings in pool boiling heat transfer are enhanced by the design of

arteries within the porous layer that promote phase separation within the layer aimed at reducing the liquid–vapor counterflow resistance. These arteries are realized in the form of modulation of the porous-layer thickness. In the example of a modulated porous-layer coating presented in this work, the vapor escape is proposed to flow out of the layer from between the modulation peaks (i.e., not internally through the porous medium). The liquid is drawn by capillarity through the tip of the modulation peaks and towards the surface through the porous medium to the location where evaporation occurs. The local regions along the coating of larger porous-layer thickness then become the liquid-flow arteries.

The goal is to enhance the q_{CHF} and the q versus $T_s - T_{lg}$ curve by using such modulated porous-layer coating systems. To reduce the number of variable parameters under consideration, this study restricts itself to atmospheric pressure, 1g, saturated pool boiling of pentane from flat horizontal copper surfaces with various modulated porous-layer coatings consisting of sintered, spherical copper particles with selected uniform diameters.

Below, the modulated porous-layer coating is described, followed by a theoretical approach to the prediction of the boiling performance of these coated surfaces, and then by a description of the experiments. Finally, the experimental results are presented, compared with the predictions, and discussed.

2. Modulated porous-layer coatings

Modulated porous-layer coatings are coatings with periodic, designed variations in layer thickness δ. The modulation is imposed to create alternating regions of low resistance to vapor escape and high capillary-assisted liquid draw. This would result in the preferential liquid–vapor counterflow paths within the layer facilitating heat transfer from the surface to the liquid pool in a manner similar to that of thermosyphons (e.g., heat pipes).

Figs. 2 and 3 show micrographs of example modulated porous-layer coatings. The coatings are made from spherical copper particles sieved within a narrow band of mesh sizes to provide near uniform particle diameters. The loose particles are consolidated (i.e., adhered) to each other and the test surface by dry-phase diffusion sintering in a tube furnace with a reducing atmosphere of Nitrogen and Hydrogen. Sintering times and temperatures varied with particle size. For particles of 200 μm nominal diameter, sintering at 1015°C for 4 h was determined to be sufficient for necking between two particles of 10–20% of the particle diameter. During sintering, the particles are held in the desired modulation shape using open-faced graphic molds. The loose particles are poured into the upward-turned open-faced molds and then the excess particles are removed to leave behind the desired uniform-thickness base layer on top. A polished-flat copper test piece substrate (taken from a 5.08 cm diameter copper round) is then inverted into the base-layer particles on the mold, and the whole mold–particles–substrate unit is placed in the furnace. After sintering, the substrate is lifted from the mold with the porous-layer coating attached.

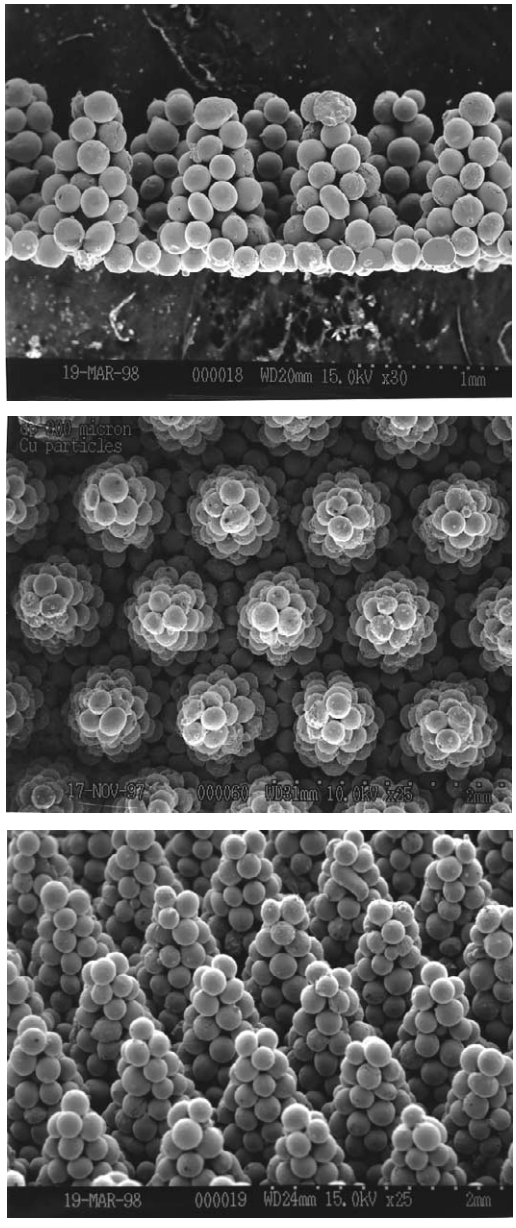

Fig. 2. SEM of single-height, modulated porous-layer coating showing (a) the side view, (b) the top view, and (c) the perspective view. The porous-layer contains spherical copper particles of diameter $d = 200$ μm molded into conical stacks.

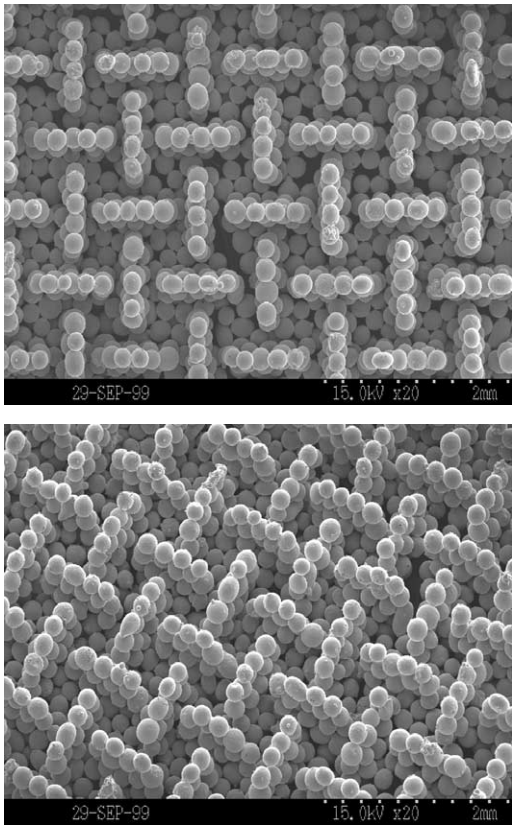

Fig. 3. SEM of single-height, modulated porous-layer coating showing (a) the top view, and (b) the perspective view. The porous-layer contains spherical copper particles of diameter $d = 200$ μm molded into tapered walls.

Various modulations of the graphite mold were machined using dicing blades and single-flute pointed drill bits with a $\theta = 20°$ taper. Mechanical limitations in the strength of the drill bit prohibited the use of smaller included-angle tapers. Modulation size limitations were also inherent in the ability of the graphite to resist flaking or chipping during machining (i.e., high aspect ratio or very thin graphite walls in the mold were not possible). These manufacturing restrictions, as well as the geometric restrictions arising from the modulation structures being nearly the same order in size as the spherical particle diameters, resulted in fabrication limits on the possible modulation length scales and designs that could be fabricated with this method. An additional and unnecessary restriction was imposed such that the modulation be divisible into repeated unit cells to simplify analytical modeling. A more complete description of the surface fabrication is given by Liter [9].

The resulting fabricated modulations consisted of either particle walls in a "waffle" pattern or of conical "stacks" of particles arranged in either square or hexagonal arrays across the surface. Preliminary results indicated that coatings consisting of the particle stacks in hexagonal arrays provided better performance. Therefore, the results of only these coatings are presented in this study.

3. Theory

It is hypothesized that the modulation in the porous-layer coating separates the liquid and vapor phases to enable capillary assisted liquid feeding to an evaporation zone with minimal resistance to vapor escape, and that two possible mechanisms exist for the choking of the liquid flow towards the surface (i.e., the q_{CHF}). In the fluid above the surface, there is a hydrodynamic liquid choking limit, $q_{CHF,h}$, that can be mechanistically related to hydrodynamic instabilities as functions of flow-critical length scales. Zuber [15] originally formulated this limit for a uniform-temperature plain surface (i.e., $q_{CHF,h} \to q_{CHF,Z}$ as $\delta \to 0$). This hydrodynamic liquid-choking limit is dependent on the fluid properties and the surface macro-scale geometry, but not the microscale surface characteristics or particle diameter. Within a porous-layer coating, the counterflow of liquid and vapor can also result in a liquid-choking limit, $q_{CHF,v}$, due to a critical viscous-drag resistance in the fluid. This viscous-drag liquid-choking limit is dependent on the fluid and coating material properties and the macro- and pore-scale geometries of the coating. The realized q_{CHF} on a surface would then correspond to the liquid-choking limit that first occurs, either above the coating due to the liquid–vapor counterflow hydrodynamics, or within the coating due to the liquid-flow viscous drag. These limits are shown in Fig. 4.

The modeling required to determine the $q_{CHF,v}$ also enables the determination of the q versus $T_s - T_{lg}$ in the wetted-surface regime prior to reaching q_{CHF}. In this section, the physical model and accompanying simplifying assumptions are presented and discussed, followed by the theory predicting the q versus $T_s - T_{lg}$, then the descriptions of the two proposed liquid-choking mechanisms.

3.1. Liquid flow and heat transfer models

To describe, predict, and optimize the liquid flow within the porous-layer coating, the flow paths to an evaporation zone must be modeled. Valid simplification of the flow paths is difficult since the complex liquid–vapor counterflow during boiling from the thin, modulated porous-layer coating is not well understood. This lack of understanding is attributed to the small range of length scales and the difficulty of visually observing the phenomena. Here, some simplifying assumptions are made with regard to the flow paths, without rigorous validation, in order to develop a model that allows for

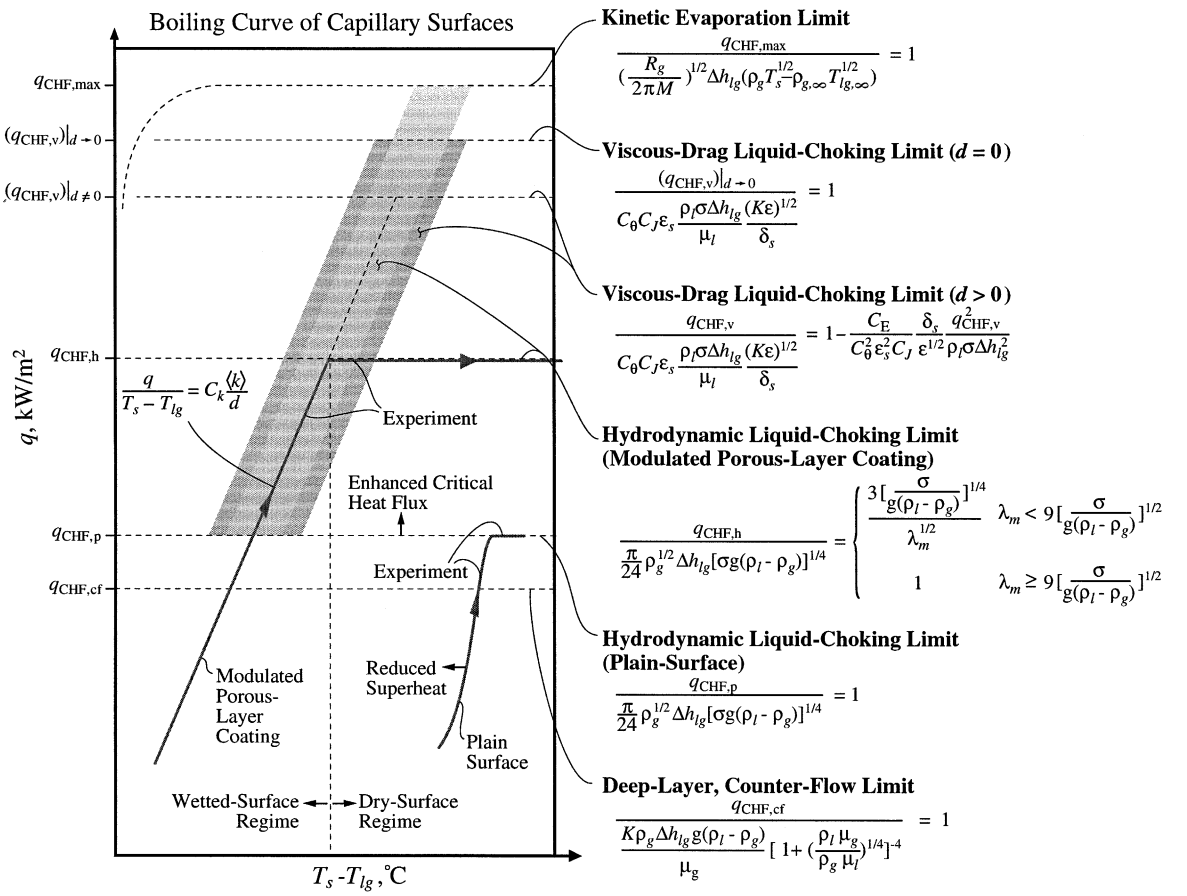

Fig. 4. A rendering of the various regimes in pool boiling with modulated porous-layer coating.

initial, qualitative study of the q versus $T_s - T_{lg}$ curve and of the viscous-drag liquid-choking limit.

Fig. 5 shows the proposed physical model for the liquid and vapor flow paths within and above a porous-layer coating with modulation in the form of conical particle stacks. This model is based on the geometry of the fabricated and experimentally tested surfaces. The stacks themselves are assumed to be porous media of uniform porosity and contained within axially symmetric frustums of right circular cones of height $\delta_s = \delta - d$ situated on top of a uniform base layer of single-particle thickness d. Local volume averaging of properties, temperature, and liquid velocity are assumed to be valid, without restriction and regardless of the particle-domain size ratio, to simplify the analysis of the transport through the particle stacks making up the modulation.

It is assumed, without visual verification, that there is complete phase separation within the coating wherefore the vapor escapes from between the stacks and the particle stacks and base layer are completely liquid saturated at all heat fluxes up to the liquid-choking limit. This appears to be reasonable considering that any

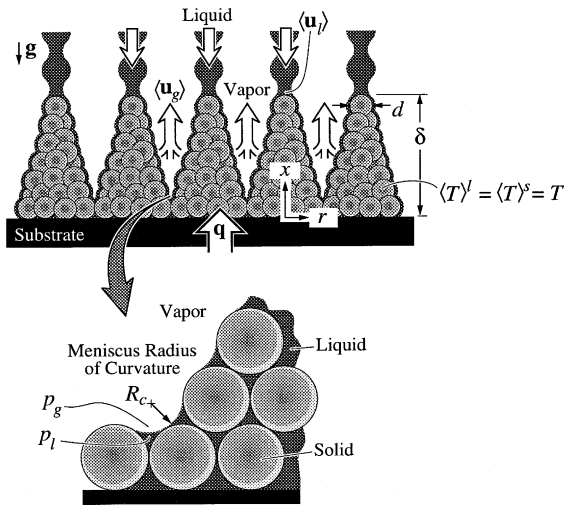

Fig. 5. A rendering of the physical model of the viscous-drag instability limit to liquid reaching the surface for the modulated porous-layer coating.

vapor within the porous matrix of the particle stacks would significantly increase the liquid-drag resistance and likely reduce the q_{CHF} to values well below those measured.

3.2. Wetted-surface regime

3.2.1. Momentum equation

Based on the preceding assumptions, the liquid is idealized as entering at the top of the stacks, and then flowing down towards the surface. The vapor pressure everywhere in the system is assumed to be constant at the saturation pressure. The flow through the stack is related to the liquid pressure drop and is modeled using the Darcy–Ergun momentum relation [16]

$$0 = -\nabla p_l + \rho_l \mathbf{g} - \frac{\mu_l}{K}\langle \mathbf{u}_l \rangle - \frac{C_E}{K^{1/2}}\rho_l \mid \langle \mathbf{u}_l \rangle \mid \langle \mathbf{u}_l \rangle, \quad (3)$$

where $\langle \mathbf{u}_l \rangle$ is the volume-averaged liquid velocity vector through the stack, K is the stack permeability, and C_E is the Ergun coefficient. The Carmen–Kozeny model is used for the permeability and results in $K = f(\epsilon)d^2 = \epsilon^3 d^2/[180(1-\epsilon)^2]$ and $C_E = (0.018/\epsilon^3)^{1/2}$. A constant stack porosity of $\epsilon = 0.4$ is assumed.

The particle stack and base layer are divided into regions and zones as shown in Fig. 6(c). It is assumed that the liquid is pumped through the stack by capillary and gravity forces to the evaporation zone.

Eq. (1) enables the determination of the temperature drop from a liquid–vapor interface to the far-field gas

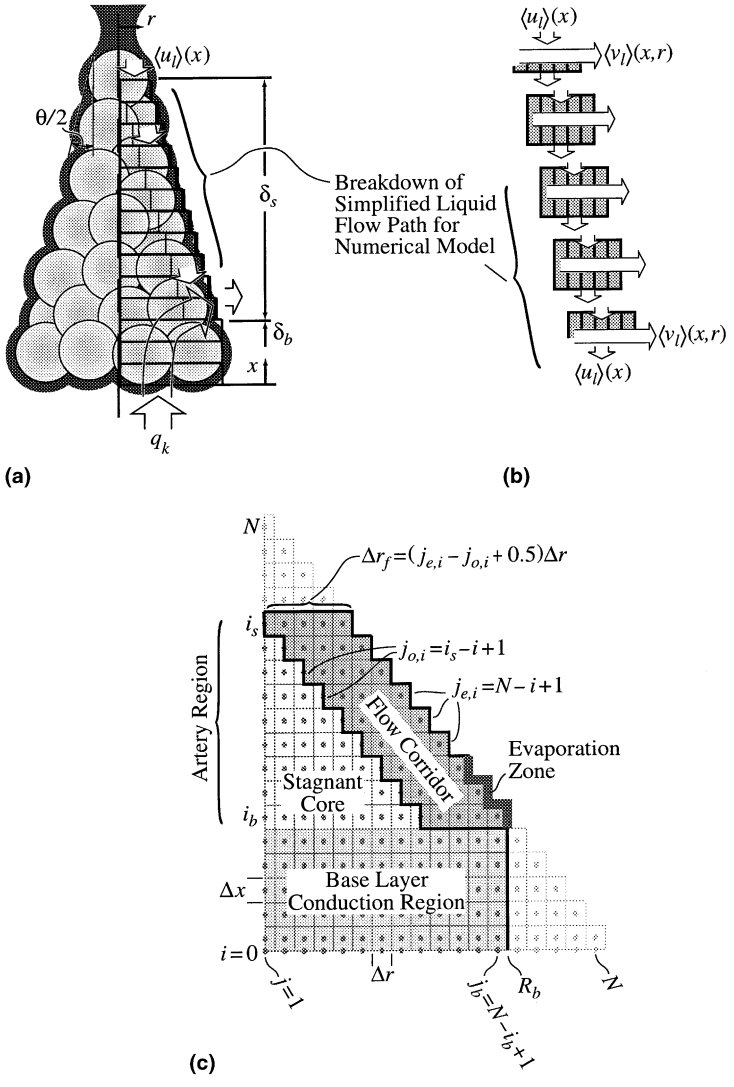

Fig. 6. Rendering of (a) the heat and liquid flow paths, (b) a schematic showing the breakdown of the liquid flow model used in the calculations, and (c) the various region designations within the particle stack and the discretized computational domain.

saturation temperature as a function of the evaporation heat flux. As an example, a $q_{\mathrm{CHF,max}} = 10^6\ \mathrm{W/m^2}$ would result in a $\Delta T = 0.28°\mathrm{C}$. This is negligible compared to the $T_s - T_{lg}$ across the porous-layer coating, and therefore the added evaporation resistance is not included in the model. The liquid is assumed to undergo thin-film evaporation, with negligible convection thermal resistance, in the evaporation zone around the perimeter of the lower part of the stacks and above the base layer.

The path of least flow resistance between the liquid entrance at the top of the stack and the location of evaporation would be nearer to the outer edge of the stack as opposed to passing through the deep interior. The benefit and likely improvement in accuracy of a fully numerically determined flow field through the stacks under the given assumptions is not large, so an approximate flow channel is assumed along a path of low flow resistance. Therefore, liquid flow is constrained to an annular flow corridor of uniform thickness $\Delta r_f = d/2$ along the side of the stack. Since the flow is assumed to occur only in the stack, the stack contains the fluid artery that feeds the evaporation. Therefore the entire stack is hereafter referred to as the artery region. The remaining interior liquid in the stack core (i.e., not in the flow corridor) and the liquid in the base layer are assumed to be stagnant. The base layer is labeled the conduction region since the heat flux must pass through the base layer by conduction to reach the evaporation zone.

The conduction and artery regions and the evaporation zone are shown in Fig. 6 along with the heat and liquid flow paths and the discretized domain used for the numerical calculations. The discretized, two-dimensional annular flow corridor in x and r is also shown. For a given row in the artery region, the first node of the flow corridor is denoted as $j_{o,i} = i_s - i + 1$, and the last node (also the outer boundary node of the row) as $j_{e,i} = N - i + 1$. The row at the top of the base layer (at the base height) is labeled i_b, while the row at the center of the topmost particle (at the stack height) is labeled i_s. For flexibility in specifying different geometries, and for ease of computation, the computational domain is a section of an $N \times N$ mesh, where each rectangular unit cell is a cross-section of a cylindrical-shell control volume. The computational unit cell facial areas are then determined as

$$A_{x\ 1} = \pi\left(\frac{\Delta r}{2}\right)^2, \quad A_{x\ j=2,N} = 2\pi r_j \Delta r,$$

$$\begin{aligned} A_{\mathrm{r}\ j=1,j_{e,i}-1} &= 2\pi\left(r_j + \frac{\Delta r}{2}\right)\Delta x, \\ A_{\mathrm{r}\ j_{e,i}} &= 2\pi\left(r_j + \frac{\Delta r}{4}\right)\Delta x. \end{aligned} \tag{4}$$

The temperature distribution in the particle stack determines the evaporation rate, which is then used to determine the required liquid supply rate (i.e., velocity distribution), as opposed to using the pressure field. The liquid mass flow is assumed to be radially lumped for a given x location. This is shown schematically in Fig. 6(b). The liquid velocity (i.e., flow) distribution is then determined from the mass flow distribution by summing the required local evaporation rates along the periphery from $i = i_b \to i_s$. For a given row i, the radial mass flow is assumed to be constant for all j and equal to that leaving through node $j_{e,i}$ by evaporation. The axial mass flow entering from the row above is then determined as the sum of all the evaporation rates at each row $i_b \to i$. Since the included cone angle is small, the direction of the mass flow from one row to the next is assumed to be in the x-direction only, and is shifted by $j + 1$ for each descending row to account for the diverging area. The velocities are then adjusted accordingly by multiplying with the area ratio $A_{x,j}/A_{x,j+1}$.

The simplified flow field is therefore determined by the evaporation rate under the imposed constraints of the localized uniform flow fields as described above, and is determined prior to calculating the pressure drop. The discretized equations determining the liquid velocities in the flow corridor are as follows.

Initializing $j_{e,i} = N - i + 1$ and $j_{o,i} = i_s - i + 1$, then for

$$i = i_b \to i_s$$

$$\begin{aligned} (\dot{M}_l)_{i,j_{e,i}} &= \frac{T_{i,j_{e,i}} - T_{lg}}{\Delta h_{lg}(R_{r,ku})_{i,j_{e,i}}}, \\ (\dot{M}_l)_{\Sigma,i} &= \left[\sum_{k=i_b}^{i-1}(\dot{M}_l)_k\right] + (\dot{M}_l)_{i,j_{e,i}}, \end{aligned} \tag{5}$$

$$A_{x,f} = \pi\left[\left(r_{j_{e,i}} + \frac{\Delta r}{2}\right)^2 - \left(r_{j_{o,i}} - \frac{\Delta r}{2}\right)^2\right], \tag{6}$$

$$j = j_{o,i} \to j_{e,i}$$

$$\begin{aligned} \langle (v_l)_{i,j}\rangle &= \frac{(\dot{M}_l)_{i,j_{e,i}}}{\rho_l}/A_{\mathrm{r}\ j}, \\ \langle (u_l)_{i,j}\rangle &= -\frac{(\dot{M}_l)_{\sum,i}}{\rho_l}/A_{x,f}, \end{aligned} \tag{7}$$

where

$$\begin{aligned} (R_{r,ku})_{i,j_{e,i}} &= \frac{\Delta r/2}{\langle k\rangle A_{\mathrm{r}\ j_{e,i}}}\,\frac{\exp((Pe_r)_{i,j_{e,i}}) - 1}{(Pe_r)_{i,j_{e,i}}\exp((Pe_r)_{i,j_{e,i}})}, \\ (Pe_r)_{i,j_{e,i}} &= \frac{\langle (v_l)_{i,j}\rangle \rho_l c_{p,l}\Delta r}{2\langle k\rangle}, \end{aligned}$$

An example of the calculated flow field is shown as a vector plot in Fig. 7.

The evaporation along the side of the stack, constituting the evaporation zone, is assumed to alter the local liquid–vapor interface to provide the corresponding interface curvature distribution for the required liquid

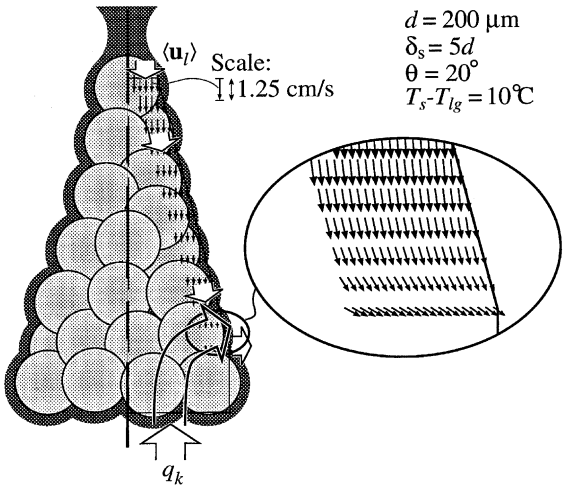

Fig. 7. A vector plot of the predicted velocity distribution $\langle \mathbf{u}_l \rangle(x)$ in the flow corridor.

capillary-pumping through the stack. There is a capillary-limiting minimum radius R_c that corresponds to the capillary pressure of the porous medium, and consequently determines the critical maximum viscous-drag resistance.

Once the flow field is determined, the resulting pressure drop across the stack is calculated and compared with the maximum available pressure drop (i.e., maximum capillary pumping). If the calculated pressure drop exceeds this maximum pressure drop, then the flow field, and consequently the temperature distribution, is considered impossible. The viscous-drag liquid choking limit is then defined as the heat flux resulting in the evaporation rate (i.e. heat flux) that requires a liquid feed rate corresponding to R_c, or in other words, it is considered to occur when the calculated pressure drop equals this maximum available pressure drop.

Therefore, the maximum sustainable pressure drop across the stack height, δ_s, is assumed to be equal to the capillary pressure, $p_c = p_g - p_l = 2\sigma/R_c$ in the porous medium of the stack. From the required velocity distribution, the resulting pressure gradient through the stack as a function of x is found from Eq. (3), and is integrated across the artery region from $d \leq x \leq \delta$ to give the total pressure drop.

Ferrel and Alleavitch [20] presented an approximation for the radius of curvature R_c of water saturating a bed of randomly packed spherical particles as $R_c = C_R d/2$, where the ratio of the largest minimum pore diameter to the particle diameter was given as $C_R = 0.41$. Assuming this expression to remain valid for pentane, in a porous medium consisting of spherical particles of $d = 200$ μm, this results in a $p_c = 698$ Pa. The capillary pressure can also be related to a capillary rise height as $p_c = \rho_l g H$. Laboratory tests using these particles with pentane resulted in a $H = 12.7$ cm, which then results in a $p_c = 760$ Pa. This would correspond to $C_R = 0.375$. The Leverett J-function relates the liquid saturation (s), porosity, permeability, and wettability to the capillary pressure through [16]

$$p_g - p_l = p_c = J(s)\frac{\sigma \cos\theta_c Z(\theta_c)}{(K/\epsilon)^{1/2}} = C_J \frac{\sigma}{(K/\epsilon)^{1/2}} \text{ for } s = 0, \tag{8}$$

where θ_c is the contact angle and is assumed negligible, $Z(\theta_c)$ is the Melrose function and is assumed unity, and $J(s)$ is the Leverett function. The capillary rise height corresponds to the case of a transition from a saturated region to a region of zero saturation (above the rise height). Therefore the maximum capillary pressure corresponds to a constant $C_J = J(s = 0)$. For the data presented by Leverett, Schiedeggar determined $C_J = 0.523$, while Udell reported a value of 0.56 [16]. Equating $p_c = 4\sigma/(C_R d)$ from Ferrel and Alleavitch, with $C_R = 0.375$, to that of Leverett in Eq. (8) results in a C_J measured for the particles of 0.53, in good agreement with the reported values. Therefore, Eq. (8) was used with $C_J = 0.53$ to determine the capillary pressure.

From the calculated velocity field, the calculated total pressure drop through the flow corridor is determined by summation of the pressure drop across each row due to an averaged axial velocity in that row, $\langle u_i \rangle_{\Delta r_f}$, which is shown schematically in Fig. 6 and determined by

$$\langle u_i \rangle_{\Delta r_f} = \frac{1}{j_{e,i} - j_{o,i} + 1} \sum_{j=j_{o,i}}^{j_{e,i}} u_{i,j}. \tag{9}$$

Then following Eq. (3), the discretized pressure equations are

$$0 = -\frac{1}{\cos(\theta/2)}\frac{\Delta p_{l,i}}{\Delta x} - \rho_l g \cos(\theta/2) - \frac{\mu \langle u_i \rangle_{\Delta r_f}}{K \cos(\theta/2)} - \frac{C_E}{K^{1/2}\cos^2(\theta/2)} \rho_l \langle u_i \rangle_{\Delta r_f} \mid \langle u_i \rangle_{\Delta r_f} \mid, \tag{10}$$

where a correction for the taper angle is included. The total pressure drop, Δp_Σ, through the flow corridor is then found by

$$\Delta p_\Sigma = \sum_{i=i_b}^{i_s} \Delta p_{l,i}. \tag{11}$$

Under the above assumptions, the model assumes that the available capillary pumping of the liquid to the evaporation zone is sufficient to sustain the evaporation rate at all heat fluxes up to the viscous-drag liquid-choking limit. At this limit (i.e., the critical heat flux $q_{CHF,v}$, the evaporation rate requires a velocity that

results in the accumulated total pressure drop being equal to the capillary pressure, i.e., $\Delta p_\Sigma = p_c$.

To determine the evaporation rates, and the resulting flow field and pressure drop across the stack, the temperature distribution must be calculated. Before discussing the model for the determination of the temperature distribution, some comments on thermal equilibrium within the stacks are presented.

3.2.2. Thermal equilibrium

The liquid and solid phases are assumed to be in local thermal equilibrium (LTE) everywhere within the particle stack since the added complexity of local non-thermal equilibrium (LNTE) is not warranted within the framework of this simplified model [19]. Although the assumption of LTE is not globally valid within the computational domain, it still enables qualitative results. Recall that in the artery region there is assumed a small stagnant core surrounded by an annulus of liquid flowing from the top of the stack to the evaporation zone through the flow corridor. The high velocities in the flow corridor result in a high Peclet number, Pe_δ, which acts to resist the flow of heat into the liquid-flow zone and to determine the thickness of the evaporation zone. The high Pe_δ indicates that the convection would dominate over the opposing conduction heat transfer processes across (up) the stack height δ, i.e., in the artery region.

The high liquid velocity also results in a large hydrodynamic dispersion term which acts to locally increase the effective thermal diffusion parameter in the flow corridor. Since the heat flux vector is (within the model assumptions) completely consumed by phase change in the small evaporation zone, increases in the local thermal diffusion parameter only within the flow corridor would have little effect on the resulting q versus $T_s - T_{lg}$ curve. This is because the strong downward convection in the artery region restricts the majority of the heat flux from penetrating too high above the conduction zone (base layer). For $Pe_d \gg 0.5$ the parallel and perpendicular dispersion coefficients can be expressed as [16],

$$\frac{D^d_\parallel}{\alpha_l} = \frac{3}{8}Pe_d + \frac{1}{12}\pi^2(1-\epsilon)Pe_d \ln\frac{Pe_d}{2},$$
$$\frac{D^d_\perp}{\alpha_l} = \frac{63}{320(2)^{1/2}}(1-\epsilon)^{1/2}Pe_d, \qquad (12)$$
$$Pe_d = \frac{(\rho c_p)_l \mid \langle u_l\rangle \mid d}{k_l} = \frac{\mid \langle u_l\rangle \mid d}{\alpha_l}.$$

For a typical velocity at $q_{CHF,v}$, $\langle u_l\rangle = 0.1$ m/s. This results in $D^d_\parallel/\alpha_l = 744.61$ and $D^d_\perp/\alpha_l = 28.78$. Since the effective volume-averaged thermal conductivity in the model is assumed isotropic, an isotropic dispersion coefficient was assumed for simplicity to be equal to the larger parallel dispersion coefficient, $D^d = D^d_\parallel$, and was included locally in the flow corridor [i.e., in each control volume (i,j) in which $(\langle \mathbf{u}_l\rangle_{i,j})$ was non-zero]. This results in only a slightly larger evaporation zone which in turn results in a negligible shift of the q versus $T_s - T_{lg}$ curve to the left in Fig. 4. The difference in the results are assumed to be well within the uncertainty of this simplified model, and therefore further refinement of the inclusion of the dispersion coefficient was considered unnecessary.

From the above discussion, the liquid and solid phases in the artery region (excluding the small evaporation zone) are assumed to be always at nearly the pentane saturation temperature, T_{lg}, and to not have large thermal gradients. Therefore, the liquid and solid phases in this region are also assumed to be in LTE.

As an alternative discussion of the validity in assuming LTE, an estimation of the NTU in the flow corridor can be made. The NTE can be defined as

$$NTU = \frac{A_{ku}\langle Nu\rangle_d k_l/d}{A_u(\rho c_p)_l \mid \langle u_{l,x}\rangle_{\delta_s} \mid}, \qquad (13)$$

where A_{ku} is the liquid–solid interfacial area for surface convection and A_u is the flow area, both in the flow corridor, and $\mid \langle u_{l,x}\rangle_{\delta_s} \mid$ is the averaged axial velocity through the flow corridor. For a randomly packed system of spherical particles with $d = 200$ μm, an assumed porosity of $\epsilon = 0.4$, a stack height of $\delta = 5d$, and an included cone angle of $\theta = 20°$, the areas would then be $A_{ku} = 1.56\times10^{-6}$ m^2, and $A_u = 8.68\times10^{-8}$ m^2. The fluid properties are listed in Table 1. To determine the $\langle Nu\rangle_d$, an empirical expression was used for surface convection through a packed bed of particles and is given as [21,22]

$$\langle Nu\rangle_d = 2 + (0.4Re_d^{1/2} + 0.2Re_d^{2/3})Pr^{0.4},$$
$$\text{where } Re_d = \frac{\rho_l \mid \langle u_{l,x}\rangle_{\delta_s} \mid d}{\mu_l(1-\epsilon)}. \qquad (14)$$

For an average velocity of $\mid \langle u_{l,x}\rangle_{\delta_s} \mid = 0.1$ m/s (typical order of magnitude of the numerical results near the

Table 1
Thermophysical properties of saturated pentane at $p_g = 1$ atm [26]

M	72.151 kg/kmol
ΔT_{lg}	36.05°C
ρ_l	610.2 kg/m^3
ρ_g	3.00 kg/m^3
Δh_{lg}	358.2 kJ/kg
σ	0.0143 N/m
μ_l	1.96×10^{-4} kg/m s
μ_g	6.9×10^{-6} kg/m s
k_l	0.107 W/m K
k_g	0.0167 W/m K
$c_{p,l}$	2340 J/kg K
Pr	4.29

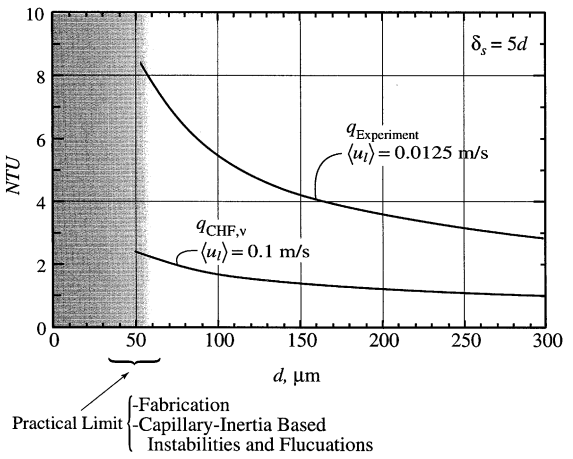

Fig. 8. The variation of NTU with respect to particle diameter d, for $\delta_s = 5d$.

predicted $q_{CHF,v}$ for this geometry), the $\langle Nu\rangle_d = 17.2$. Then the $NTU = 1.2$. This would indicate that the heat exchanger effectiveness of the flow corridor is around 0.6 at this theoretical operating condition and that LTE would not be a valid assumption. Evaluating the NTU at more realistic operating conditions of $|\langle u_{l,x}\rangle_{\delta_s}| = 0.0125$ m/s (determined from the numerical model for $T_s - T_{lg} = 10°C$), the $\langle Nu\rangle_d = 6.6$ resulting in an $NTU = 3.5$. This would indicate that the heat exchanger effectiveness of the flow corridor is near unity and LTE would be a valid assumption. As the heat flux (and correspondingly the $T_s - T_{lg}$) decreases, the average liquid velocity decreases resulting in a longer residence time of the liquid in the flow corridor allowing the liquid and solid phases to reach LTE. This would indicate that the assumption of LTE becomes more valid the further the system operates in the wetted-surface regime away from the q_{CHF} point. This analysis does not include the effect of the evaporation at the end of the flow corridor consuming the incoming heat flux. Fig. 8 shows the variation of NTU versus particle diameter for constant δ_s/d, $|\langle u_{l,x}\rangle_{\delta_s}|$, and fluid properties. This plot indicates that the assumption of LTE becomes increasingly valid with decreasing d.

In the conduction zone, the liquid is assumed to be stagnant, and at steady state conditions and neglecting thermobuoyant motion, the liquid and solid phases here can be assumed to be in LTE as well. The assumption of LTE within the evaporation zone is least valid, but since this zone constitutes such a small part of the domain, the invalidity of the assumption negligibly affects the predictions.

3.2.3. Energy equation

Assuming LTE, the temperature distribution is modeled following

$$\nabla\cdot[(\rho c_p)_l\langle\mathbf{u}_l\rangle\langle T\rangle - (\langle k\rangle + \langle k\rangle^d)\nabla\langle T\rangle] = \begin{cases} 0, & r_j < r_{j_{e,i}} \\ \nabla\cdot(\rho_l\langle\mathbf{u}_l\rangle\Delta h_{lg}), & r_j = r_{j_{e,i}}, \end{cases} \quad (15)$$

which can be non-dimensionalized and scaled with δ as

$$\nabla\cdot[Pe_\delta\mathbf{u}_l^* T^* + (1+\frac{\langle k\rangle^d}{\langle k\rangle})\nabla T^*] = \begin{cases} 0, & r_j < r_{j_{e,i}} \\ \nabla\cdot(Pe_\delta\mathbf{u}_l^*/Ja, & r_j = r_{j_{e,i}}, \end{cases} \quad (16)$$

where

$$Pe_\delta = \frac{(\rho c_p)_l\delta\,|\,\langle u_l\rangle\,|_{\theta=0}}{\langle k\rangle}, \quad Ja = \frac{c_{p,l}(T_s - T_{lg})}{\Delta h_{lg}},$$

$$T^* = \frac{\langle T\rangle - T_{lg}}{T_s - T_{lg}}, \quad \mathbf{u}_l^* = \frac{\langle\mathbf{u}_l\rangle}{|\,\langle u_l\rangle\,|_{\theta=0}}$$

and where $\langle T\rangle$ is the local volume-averaged temperature, $\langle k\rangle$ is the volume-averaged effective stagnant thermal conductivity, $\langle k\rangle^d = (\rho c_p)_l D^d$ is the dispersion contribution to the total thermal conductivity ($\langle k\rangle + \langle k\rangle^d$), $|\langle u_l\rangle|_{\theta=0}$ is a constant for a given q and is the maximum velocity corresponding to a cylindrical stack, and the evaporation term (right-hand side of the equation) is assumed zero everywhere except on the side boundaries of the stack. The volume-averaged stagnant thermal conductivity is assumed constant and is predicted to be $\langle k\rangle = 9$ W/m^2 K by the modified Zehner–Schlunder model [23] accounting for a $0.15d$ sintered contact area, and using an assumed porosity of $\epsilon = 0.4$.

The upwards heat flux is in part resisted by the downwards convection due to the liquid flow in the stack within the annular flow corridor. At the liquid–vapor interface along the periphery of the bottom of the stack (i.e, at the top of the base layer at $x = d$), the heat flux begins to be consumed by evaporation. The heat flux rising through the stack then diminishes to zero at some height as it is completely consumed. The model predicts this height to be on the order of magnitude less than one particle radius from the base of the stack.

The temperature distribution must be calculated to determine the evaporation rates, and the resulting flow field and required pressure drop, in order to predict the $q_{CHF,v}$. The temperature distribution is determined using the discretized finite-volume form of Eq. (15). The boundary conditions for the system are an evaporation heat flux to a constant vapor temperature $T_g = T_{lg}$ on the side of the stacks [$r(x)$ from $i_b < i < i_s$], an insulated vertical side through the symmetry plane in the base layer [$r(x) = R_b$ from $0 < i < i_b - 1$], a constant saturation temperature on the top ($j, i = i_s$), and a constant input heat flux at the bottom surface ($j, i = 0$). The temperature distribution is therefore predicted as a function of the input surface heat flux. The surface superheat is then determined for each prescribed flux as

the area-averaged predicted base temperature $T_s - T_{lg} = \langle T \rangle |_{x=0}$. The discretized energy conservation equations are given in the appendix.

3.2.4. Slope of wetted-surface regime

It is assumed that at all heat fluxes below that resulting in the viscous-drag choking limit, there exists sufficient liquid pumping through the flow corridor to the evaporation zone to feed the liquid–vapor phase change. Since the resistence for evaporation is assumed negligible, the phase change effectively consumes all of the heat flux within a short evaporation zone, on the order of less than $0.5d$, above which the volume-averaged temperatures would be equal to the saturation temperature T_{lg}. Below the evaporation zone, in the base layer, the heat flux is assumed to be by conduction only. Calculations predict that the heat flux through the base layer is indeed nearly one-dimensional in the x-direction, before converging towards the evaporation zone at the top of the base layer. This can be seen from the example plots of the calculated temperature profiles shown in Fig. 9. Therefore, assuming a linear temperature profile from the surface to the evaporation zone, to approximate a one-dimensional heat flux, a characteristic length, $L_k = d/C_k$ (where C_k is a correction factor), would exist that would account for the thickness of the base layer (if $\delta_b > d$), the effect of the cylindrical geometry, the turning of the heat flux towards the evaporation zone (peripheral surface), plus an additional average effective height above the top of the base layer and into the evaporation zone. The heat flux in the wetted-surface regime can then be approximately related to the surface superheat, $T_s - T_{lg}$, by

$$\frac{q}{T_s - T_{lg}} = \frac{\langle k \rangle}{L_k} = C_k \frac{\langle k \rangle}{d}. \tag{17}$$

Since the geometry is scaled with d, C_k is independent of particle size for a given geometry. For a conical stack geometry, C_k is dominantly dependent on the aspect ratio of the base layer, i.e., the height of the base layer δ_b, and the base diameter of the stack, $2R_b$. The base diameter is characterized by the stack height, δ_s, and the included angle of the cone, θ. Therefore, the functional dependence of the conduction coefficient is approximated as $C_k = f(\delta_s/d, \theta, \delta_b/d)$. For a base layer of height $\delta_b = 1d$, the constant C_k would be expected to be slightly less than unity (i.e., L_k is expected to be slightly greater than δ_b). Solving the numerical model for q as a function of $T_s - T_{lg}$, a constant value of $C_k = 0.82$ was found for this conical stack geometry characterized by $\theta = 20°, \delta_s = 4d,$ and $\delta_b = d$.

From Eq. (17), the q versus $T_s - T_{lg}$ curve in the wetted-surface regime prior to the critical heat flux can be calculated and plotted as shown in Fig. 4.

3.3. Viscous-drag liquid-choking limit

As mentioned, the evaporation along the side of the stack requires a certain rate of liquid supply which determines the liquid velocity distribution $\langle \mathbf{u}_l \rangle (x)$. As the evaporation (i.e., heat flux) is increased, the liquid flow must increase. This results in an increased viscous-drag resistance within the particle stack. The viscous-drag liquid-choking limit is then determined by a balance between the rate of liquid evaporation and the ability for the liquid to be resupplied through the stack. These flow paths were shown in Fig. 5.

Recall that the liquid is assumed to be pumped through the artery region by capillary and gravity forces. The evaporation along the side of the stack is assumed to alter the local liquid–vapor interfaces to provide the required interface curvature distribution for the liquid capillary-pumping through the stack. There then exists a capillary-limiting minimum radius R_c that corresponds to the capillary pressure for the porous media, and consequently determines the critical-maximum viscous-drag resistance. The viscous-drag liquid choking limit is then defined as the heat flux resulting in the evaporation rate (i.e. heat flux) that requires a liquid feed rate corresponding to $-\mathrm{d}p/\mathrm{d}x = p_c/\delta_s$.

The viscous-drag liquid-choking limit (i.e., the critical heat flux $q_{CHF,v}$) is then considered to be at the flux requiring a velocity that results in the pressure drop being equal to the capillary pressure, i.e., $\Delta p_\Sigma = p_c$.

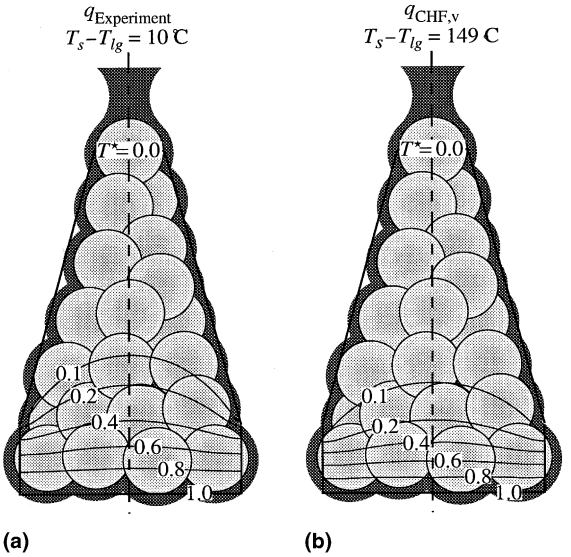

Fig. 9. A contour plot of the predicted temperature distribution within the base layer and the particle stack for (a) $T_s - T_{lg} = 10°C$ corresponding to the typical magnitude of the measurements, and (b) $T_s - T_{lg} = 149°C$ corresponding to the predicted (i.e. theoretical) $q_{CHF,v}$.

Instead of the numerical model, an analytical approximation for the $q_{\mathrm{CHF,v}}$ can be found by making a few further simplifications. Assuming that the effect of variable flow area (i.e., assuming cylindrical instead of conical stacks, $\theta \to 0$) is negligible, and that all of the liquid flows one-dimensionally the full length δ_s through the flow corridor before evaporating, then the pressure gradient through the vertical flow corridor would be linear. Further, assuming the effect of gravity is negligible, and using a characteristic length scale of $K^{1/2}$, and noting $u(x) < 0$, then Eq. (10) can be simplified for a one-dimensional system to be

$$0 = -\frac{\mathrm{d}p^*}{\mathrm{d}x^*} + Ca + We_{K^{1/2}} \qquad (\theta = 0), \tag{18}$$

where $\mathrm{d}p^*/\mathrm{d}x^*$ is a dimensionless and normalized pressure gradient, and where We is the Weber number and Ca is the capillary number, each defined as

$$\begin{aligned} We_{K^{1/2}} &= \frac{\rho_l \langle u_l \rangle^2 K^{1/2}}{\sigma} \frac{C_E \delta_s}{C_J (K\epsilon)^{1/2}}, \\ Ca &= \frac{|\langle u_l \rangle| \mu_l}{\sigma} \frac{\delta_s}{C_J (K\epsilon)^{1/2}}, \quad C_J = 0.53. \end{aligned} \tag{19}$$

In Eq. (18), the solution would indicate the maximum velocity achievable by the available capillary pumping power. This velocity would not be that experienced within the experimental stack, but rather represents an upper limit that is dependent on the permeability and stack height, $K(d)$ and $\delta_s(d)$, and therefore on the particle size, d. Note that this theoretical limit is determined solely in the artery region (i.e., stack), and is independent of base layer thickness, δ_b. In this model, variations in δ_b would be realized through C_k and the resulting shifting of the q versus $T_s - T_{lg}$ curve to the right or left. The velocity in the stack can then be classified as a fraction of this maximum velocity (corresponding to a maximum viscous-drag liquid-choking limit, $(q_{\mathrm{CHF,v}})_{\theta=0}$), where the ratio would depend on the stack geometric parameters such as the included cone angle.

The velocity, $\langle u_l \rangle$, can be written in terms of the critical heat flux and an area fraction, ϵ_s, defined as the ratio of the cone-base area to the unit-cell surface area, as

$$\langle u_l \rangle = \frac{(q_{\mathrm{CHF,v}})_{\theta=0}}{\epsilon_s \rho_l \Delta h_{lg}}. \tag{20}$$

The cone-base area to unit-cell surface area ratio, ϵ_s, is included to account for the different patterns of the stack modulations across the surface. For example, for adjacent single-height stacks in a square array, $\epsilon_s = \pi/4 = 0.785$, and for an hexogonal array, $\epsilon_s = 3^{1/2}\pi/6 = 0.907$.

Recursively solving Eq. (18) for u through the flow corridor, and substituing Eq. (20) for u, an expression for the maximum viscous-drag liquid-choking limit, $(q_{\mathrm{CHF,v}})_{\theta=0}$, can be found as

$$\frac{(q_{\mathrm{CHF,v}})_{\theta=0}}{\epsilon_s C_J (\rho_l \sigma \Delta h_{lg}/\mu_l)((K\epsilon)^{1/2}/\delta_s)} = 1 - \frac{C_E}{C_J} \frac{\delta_s}{\epsilon_s^2 \epsilon^{1/2}} \frac{(q_{\mathrm{CHF,v}})_{\theta=0}^2}{\rho_l \sigma \Delta h_{lg}^2}. \tag{21}$$

In this recursive form, the effect of particle diameter on the $(q_{\mathrm{CHF,v}})_{\theta=0}$ can be seen. Since the stack height, δ_s, and the square root of permeability, $K^{1/2}$ are assumed each directly proportional to d, the effect of d is consolidated into the second term of the right-hand side of Eq. (21). As $d \to 0$, then the right-hand side of Eq. (21) equals unity. Eq. (21) was scaled with the solution to the viscous limit of Eq. (18), namely the solution to $Ca = \mathrm{d}p^*/\mathrm{d}x^*$. Therefore, as d decreases, viscous forces dominate over inertial forces, and in the limit, a maximum $q_{\mathrm{CHF,v}}$ exists as

$$\begin{aligned} (q_{\mathrm{CHF,v}})_{\theta=0} &= \epsilon_s C_J \frac{\rho_l \sigma \Delta h_{lg}}{\mu_l} \frac{(K\epsilon)^{1/2}}{\delta_s} \\ &= \frac{We_{K^{1/2}}}{Ca^2} \frac{\mu_l \Delta h_{lg}}{C_E K^{1/2}} \qquad d \to 0. \end{aligned} \tag{22}$$

Eq. (20) can be used with Eq. (18) to also explicitly solve for $(q_{\mathrm{CHF,v}})_{\theta=0}$ as

$$\begin{aligned} \frac{(q_{\mathrm{CHF,v}})_{\theta=0}}{(We_{K^{1/2}}/Ca^2)(\mu_l \Delta h_{lg}/C_E K^{1/2})} &= -\frac{1}{2(We_{K^{1/2}}/Ca^2)} \\ &+ \left[\left(\frac{1}{2(We_{K^{1/2}}/Ca^2)} \right)^2 + \frac{1}{We_{K^{1/2}}/Ca^2} \right]^{1/2}. \end{aligned} \tag{23}$$

For cases when $\theta > 0$, a coefficient $0 < C_\theta(\theta) \leqslant 1$ can be used to adjust the maximum velocity found in Eq. (18) to account for the effect of variable flow area (i.e., conical sidewalls as opposed to a cylindrical stack), as computed with the numerical model. Therefore, the unit-cell critical heat flux (i.e., surface viscous-drag liquid-choking limit), corresponding to the $q_{\mathrm{CHF,v}}$ calculated from the model, can be approximated as

$$q_{\mathrm{CHF,v}} = C_\theta (q_{\mathrm{CHF,v}})_{\theta=0}, \tag{24}$$

where C_θ is an empirical function of θ found by taking the ratio as a function of θ of the numerical results and that predicted by Eq. (23). The function C_θ was found to be negligibly dependent on d within the range of interest $50\ \mu\mathrm{m} \leqslant d \leqslant 200\ \mu\mathrm{m}$ at various θ. The variation of C_θ versus θ, as determined from the results of the numerical model, is shown in Fig. 10.

The viscous-drag liquid-choking model presents a means of determining the q versus $T_s - T_{lg}$ relationship and the $q_{\mathrm{CHF,v}}$ corresponding to the theoretical viscous-drag liquid-choking limit within the stack. It is highly dependent on the model used for treating the porous medium as well as the assumed simplified liquid-flow paths, but as a first approach, it appears to have

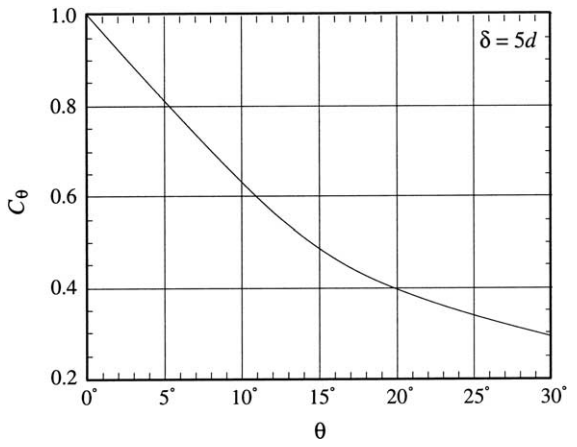

Fig. 10. The calculated variation of the coefficient C_θ as a function of included angle of a conical stack (for 50 μm $\leqslant d \leqslant$ 300 μm).

qualitative agreement with the experimental results to be presented.

3.4. Hydrodynamic liquid-choking limit

A hydrodynamically determined liquid-choking limit $q_{\mathrm{CHF,h}}$ has been proposed in addition to $q_{\mathrm{CHF,v}}$. The modulated porous-layer coating can create designed (non-hydrodynamically determined) locations of vapor escape into the liquid pool altering the thermal-hydraulics in the pool and above the layer, thus extending the classical hydrodynamic liquid-choking limit. This model, therefore, considers the ability for the liquid to flow towards the surface through the escaping vapor.

Zuber [15] developed a mechanistic theoretical model for the q_{CHF} based on idealized hydrodynamics of a liquid–vapor interface system above the surface. Idealizing the vapor flow, he equated the boiling heat transfer Q to the rate of heat escape by buoyant flow of the vapor through the liquid as

$$Q = \rho_g u_g h_g A_g, \tag{25}$$

where A_g is the cross-sectional flow area for vapor escape above a representative (spatial periodicity assumed) portion of the surface. Then the maximum heat transfer Q_{CHF} was when the vapor enthalpy approached the latent heat resulting in an expression for q_{CHF} as

$$q_{\mathrm{CHF}} = \frac{Q_{\mathrm{CHF}}}{A_b} = \rho_g u_g \Delta h_{lg} \frac{A_g}{A_b}, \tag{26}$$

where A_b is the base surface area of a representative cell beneath A_g, i.e., $A_b = A_g + A_l$. Fig. 11 shows a rendering of the determination of A_g and A_b. Zuber hypothesized that the base surface area A_b corresponds to a periodic cell determined by a flow-critical, base length scale λ_b of the fluid, i.e., $A_b = \lambda_b^2$. From the spacing determined by λ_b, the vapor bubbles would then flow from the surface (i.e., break through the liquid) through idealized cylindrical vapor-flow channels of area $A_g = \pi R_g^2$, where radius $R_g = a\lambda_b$, and where a is the to be determined ratio of R_g/λ_b. In this idealized model, as the heat flux is increased, the vapor velocity increases until the liquid–vapor interface of the channel walls becomes unstable. For a vapor flowing adjacent to a liquid with the liquid–vapor interface parallel to gravity, the critical-flow length scale along the interface as a function of vapor velocity corresponds to the Kelvin–Helmholtz instability wavelength as [15]

$$\lambda_{\mathrm{KH}} = \frac{2\pi\sigma}{\rho_g u_g^2} \quad \text{or} \quad u_g = \left(\frac{2\pi\sigma}{\lambda_{\mathrm{KH}}\rho_g}\right)^{1/2}. \tag{27}$$

Substituting Eq. (27) into Eq. (26), we obtain

$$q_{\mathrm{CHF}} = \rho_g \Delta h_{lg} \left(\frac{2\pi\sigma}{\lambda_{\mathrm{KH}}\rho_g}\right)^{1/2} \frac{\pi a^2 \lambda_b^2}{\lambda_b^2} = \Delta h_{lg} \left(\frac{2\pi^3 a^4 \sigma \rho_g}{\lambda_{\mathrm{KH}}}\right)^{1/2}. \tag{28}$$

The λ_{KH} and a must then be determined to evaluate the q_{CHF} with Eq. (28). From a capillary energy analysis, Rayleigh determined that for a fluid jet of diameter $2R$, the flow-critical length scale corresponding to destabilization is equal to the jet circumference, i.e., the Rayleigh wavelength $\lambda_R = 2\pi R$ [24]. Zuber then equated the Kelvin–Helmholtz and Rayleigh wavelengths as $\lambda_{\mathrm{KH}} = \lambda_R = 2\pi R_g = 2\pi a \lambda_b$. This form still requies the proper determination of λ_b and a. In the work of Zuber, for boiling on a plain surface, the λ_b was assumed to develop from the condition of the vapor being generated on the surface but underneath the liquid pool. For a liquid–vapor interface system in which a more dense fluid is above a less dense fluid with respect to gravity, the critical instability wavelengths λ_b would arise from a balance of surface tension and buoyancy and would result in either the most critical (largest disturbance) or most dangerous (fastest growing disturbance) Rayleigh–Taylor instability wavelength, $\lambda_{\mathrm{RT,c}}$ or $\lambda_{\mathrm{RT,d}} = 3^{1/2}\lambda_{\mathrm{RT,c}} = 3^{1/2} 2\pi\{\sigma/[g(\rho_l - \rho_g)]\}^{1/2}$. After separately substituting both of these wavelengths into Eq. (28), Zuber simplified the two results into his well-known relation for the critical heat flux from plain surfaces by compromising on an intermediate value of $\lambda_b = (9/2\pi)\lambda_{\mathrm{RT,c}}$. He then set $\lambda_{\mathrm{KH}} = 2\pi a \lambda_b = 9a\lambda_{\mathrm{RT,c}}$ to obtain

$$\frac{q_{\mathrm{CHF,Z}}}{\rho_g^{1/2}\Delta h_{lg}\left[\sigma g\left(\rho_l - \rho_g\right)\right]^{1/4}} = \frac{\pi}{24}, \tag{29}$$

where, also for simplicity, he chose $a = 1/4$.

Lienhard and Dhir [25] argued from experimental observation that the $\lambda_{\mathrm{RT},d}$ would be the dominating flow-

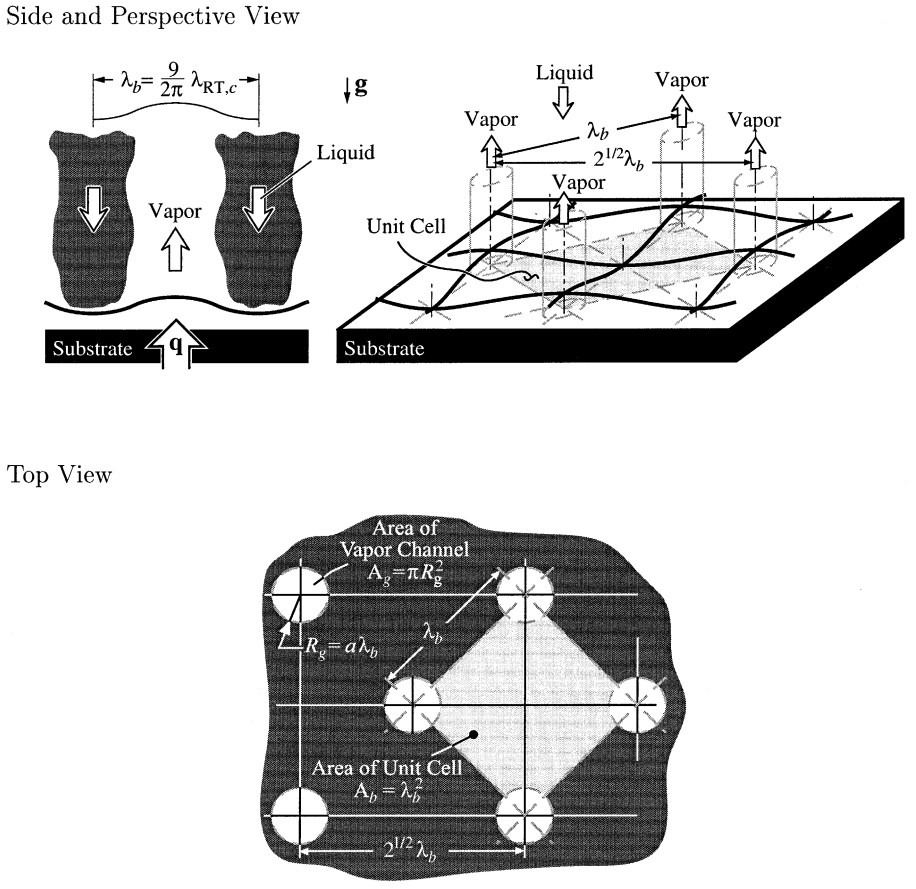

Fig. 11. Rendering of the geometry for the liquid and vapor counterflows showing the spacing for the vapor escape into the liquid pool.

critical length scale along the surface, and that for infinite surfaces, these waves would continue into the vapor channels, thus effecting the destabilization of the channel walls before the Rayleigh waves. They suggested as a better choice to set $\lambda_b = \lambda_{KH} = \lambda_{RT,d} = 3^{1/2}\lambda_{RT,c}$ resulting in a value 1.14 times higher than that predicted by Eq. (29).

These determinations of λ_b ignore the presence of any protuberances into the liquid–vapor interface that might delay the development of the λ_{RT}, thus prolonging the wetting of the surface by allowing the liquid to break through. We hypothesize that the modulation of the porus-layer thickness (i.e., introduction of protuberances), imposes a geometrically determined critical length scale λ_m, correspnding to the modulation wavelength, λ_b, that supersedes the dependence on the Rayleigh–Taylor wavelength and extends the hydrodynamic liquid-choking limit. The modulation therefore delays surface dryout and extends the q_{CHF} to where a stable flow-critical wavelength can be estabilished between two protuberances. Fig. 12 shows a rendering of the physical model for the hydrodynamic instability limit to liquid reaching the surface for both the porous-layer coating and a plain surface. Measurements of the q_{CHF} from a plain surface performed for this study had good agreement with Eq. (29). Therefore, using Zuber's approach with $a = 1/4$ and setting $\lambda_{KH} = 2\pi a\lambda_b = 2\pi a\lambda_m$, Eq. (28) then becomes

$$\frac{q_{CHF,h}}{(\pi/24)\rho_g^{1/2}\Delta h_{lg}\left[\sigma g(\rho_l-\rho_g)\right]^{1/4}} = \left(\frac{9}{2\pi}\frac{\lambda_{RT,c}}{\lambda_m}\right)^{1/2} = \frac{3\left[\sigma/g(\rho_l-\rho_g)\right]^{1/4}}{\lambda_m^{1/2}}, \tag{30}$$

or more simply

$$q_{CHF,h} = \frac{\pi}{8}\Delta h_{lg}\left(\frac{\sigma\rho_g}{\lambda_m}\right)^{1/2},$$

where the subscript h distinguishes this q_{CHF} as the hydrodynamic liquid-choking limit (as opposed to the

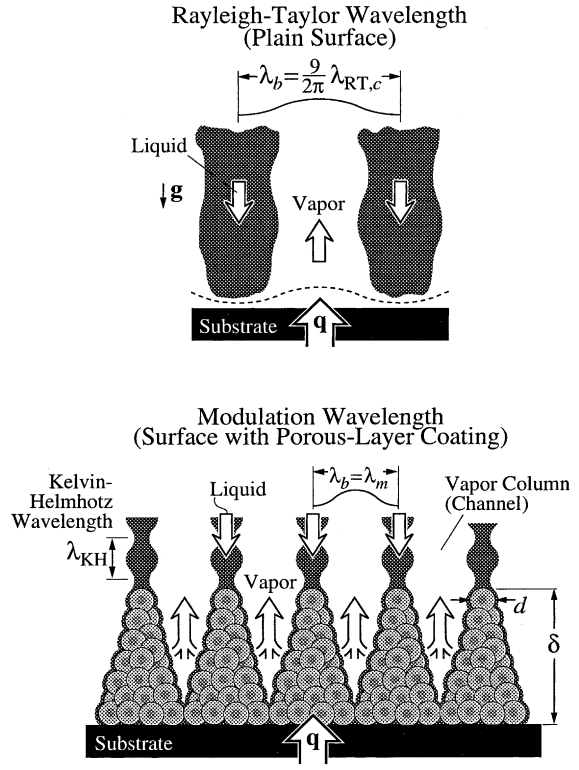

Fig. 12. A rendering of the physical model of the hydrodynamic instability limit to the liquid reaching the surface, for a plain surface, and for a surface with a modulated porous-layer coating.

viscous-drag liquid-choking limit), and where $\lambda_b = \lambda_m$ is now assumed to correlate with the dominating mechanism for determining the vapor-escape spacing along the surface. For the modulated porous-layer coated surface, λ_m corresponds to the macro-scale geometry (i.e., a modulation wavelength).

The liquid and vapor exchange in and above a uniform coating, i.e., not having preferential paths provided by modulation of the coating or by some other means, would be characterized by a random distribution of vapor escape from a fraction of the pores into the liquid pool above the layer. It has been suggested that a corresponding $\lambda_m = \lambda_u$ for a uniform coating could be determined using statistical empiricism for the vapor escape locations, along with a means of accounting for the liquid–vapor counterflow within the layer such as a percolation theory or the concept of a breakthrough pressure [12]. Using the concept of the breakthrough pressue along with a statistical pore-size distribution for a wide range of experimental data, Polezhaev and Kovalev modified the hydrodynamic Zuber theory to suggest an expression with two empirical constants for the thin uniform porous-layer coating critical heat flux, $q_{CHF,u}$, as [12]

$$q_{CHF,u} = 0.52\epsilon^{2.28}\Delta h_{lg}\left[\frac{\sigma\rho_l\rho_g}{(\rho_l+\rho_g)R_{br}}\right]^{1/2},$$

where R_{br} is the measured breakthrough pore radius. Assuming $R_{br} = d/2$ and $\rho_l/(\rho_l+\rho_g) = 1$, this can be rewritten in the form of Eq. (30) as

$$\frac{q_{CHF,u}}{(\pi/24)\rho_g^{1/2}\Delta h_{lg}\left[\sigma g(\rho_l-\rho_g)\right]^{1/4}} = \frac{3\left[\sigma/g(\rho_l-\rho_g)\right]^{1/4}}{\lambda_u^{1/2}}, \tag{31}$$

where

$$\lambda_u = \left(\frac{\pi}{5.88\epsilon^{2.28}}\right)^2 d.$$

Note that here, as is the case for the modulated porous-layer coating, λ_u is a function of geometry and structure only, and is independent of thermophysical properties [except whereas they might affect the R_{br} which was here assumed as $R_{br} = R_{br}(d)$].

Fig. 13 shows the variation of $q_{CHF,h}$ with λ_m following Eq. (30) for pentane as the working fluid. Also shown in the figure are the experimental measurements. The upper limit of λ_m for it to still affect the $q_{CHF,h}$ is $\lambda_m \to (9/2\pi)\lambda_{RT,c}$, because this is where the $q_{CHF,h} \to q_{CHF,Z}$. The $q_{CHF,h}$ increases proportionally with $\lambda_m^{-1/2}$ as λ_m is reduced from $(9/2\pi)\lambda_{RT,c}$. There exists a λ_m for optimum $q_{CHF,h}$, below which a larger λ_b will begin to develop over the top of the protuberances resulting in a decrease in the q_{CHF}. The optimum $\lambda_m = \lambda_{m,min}$ is considered to be a function of a liquid-column (channel) curvature limit which depends on the porous-medium particle diameter d, fluid properties, and coating thickness δ. In the limit of $\lambda_m \to d$, the modulation effectively vanishes and the coating becomes a uniform porous-

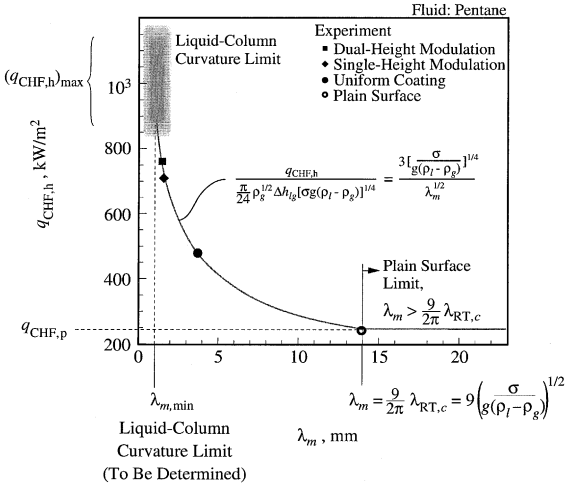

Fig. 13. Variation of the predicted $q_{CHF,h}$ with respect to the modulation wavelength λ_m.

layer coating with its accompanying lower enhancement in q_{CHF}. Determination of the optimum $\lambda_m = \lambda_{m,min}$ is yet to be done.

4. Experiment

As mentioned above, a method for fabricating the porous-layer coatings with designed modulation was developed. This method was previously described with more detail, along with the experimental setup and procedure, by the authors [18]. A brief description is repeated here. Experiments were performed at atmospheric pressure using pentane as the liquid and copper as the surface and coating-particle material. The pentane saturation properties used are listed in Table 1.

Coatings were fabricated from monosized, spherical copper particles, as described in Section 2, and were applied to a solid, planar copper test surface of $d = 5.08$ cm. The hydrodynamic model of Zuber [15] and the extensions developed here assume an infinite surface dimension. Lienhard and Dhir [25] experimentally showed that there is a minimum number of escaping vapor locations spaced $\lambda_b (= \lambda_{RT,d}$ for a plain surface) across a surface before it can be approximated as infinitely large and edge effects can be neglected. They showed that the criterion for such an approximation is that the characteristic dimension of the surface (e.g., the test surface diameter, d_s) must be at least three times the $\lambda_{RT,d}$ or $d_s \geqslant 3\lambda_{RT,d}$. For our testing surface and liquid, $\lambda_{RT,d} = 1.69$ cm and $d_s/\lambda_{RT,d} = 5.08/1.69 = 3.01$, so the test surfaces were assumed to behave as infinite surfaces. To better approximate the boiling from an infinite flat surface, a short glass cylindrical tube was positioned in the liquid pool around the circular test surface to prevent lateral entrainment of liquid due to the buoyant convection of the vapor.

The coated test surfaces were attached to a large, cylindrical, insulated copper thermal mass by the use of clamping plates. A silver grease was used to reduce the thermal contact resistance. A glass reservoir and a steel base plate were fabricated to seal around the test surface and to hold the liquid pool. A copper-pipe condensor was used to condense the vapor, and a flexible plastic cap was used to close the system and to maintain atmospheric pressure. Joulean heaters were used to heat the lower half of the insulated copper thermal mass. The insulation directed the heat transfer through the top half of the thermal mass and then through the test piece. Six Type E thermocouples were aligned axially at measured locations, three in the thermal mass and three in the test piece. These were used to determine the heat flux through Fourier's Conduction Law. The surface temperature underneath the porous coating was determined by extrapolation of the heat flux through the thermocouples in the test piece. Estimating the uncertainties in the property values to be 0.5%, in the thermocouples to be 1.7°, and in the position measurements to be 0.05 cm, the uncertainty in the heat flux at the critical point was determined to be on the order of magnitude of 5%, and in the extrapolated surface temperature on the order of 7%. Note that the percent uncertainty in the heat flux measurement would increase with decreasing heat flux due to the associated smaller ΔT.

The Q and $T_s - T_{lg}$ were measured after the system reached quasi-steady state conditions (local-time-average temperatures at each thermocouple location did not vary for 5 min) at intervals of increasing heat input, the intervals becoming smaller as q_{CHF} was approached. The q_{CHF} was said to have occurred at the last quasi-steady state measurement interval before the transition to film boiling was observed. This observation was noted as a sudden runaway transient temperature increase.

Different porous layers were constructed with various porous-layer overall thickness ranging between 1 and 9 particle diameters, and various modulations creating uniformly spaced hexagonal unit cells ranging in size from 5 to 15 particle diameters. Only the two modulated

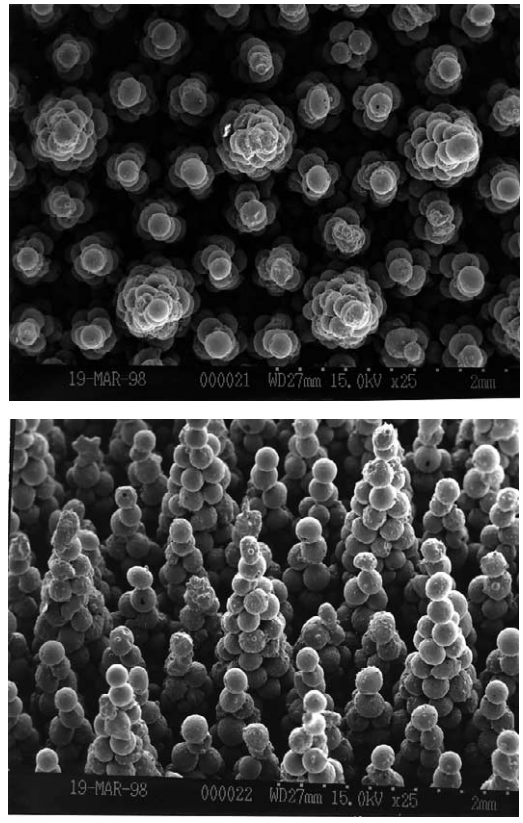

Fig. 14. SEM of dual-height, modulated porous-layer coating showing (a) the top view, and (b) the perspective view. The porous-layer contains spherical copper particles of diameter $d = 200$ μm molded into conical stacks.

porous-layer coatings exhibiting the best enhancement are presented here. They are listed below:

(i) A coating of single-height modulated conical stacks fabricated with $\delta = 6d$, and $\lambda_b = 5d (d = 200\ \mu m)$. This surface is shown in Fig. 2.

(ii) A coating of dual-height modulated conical stack groups consisting of a tall stack of $\delta = 9d$ surrounded by six shorter stacks of $\delta = 5d$, and a peak-to-peak tall-stack spacing of $\lambda_b = 8d (d = 200\ \mu m)$. This surface is shown in Fig. 14.

5. Results and discussion

5.1. Measurements

Repeatable results for a number of surfaces with various porous-layer coating modulations have been obtained for the heat flux q versus the surface superheat $T_s - T_{lg}$ up to the critical heat flux q_{CHF}. Fig. 15 shows four experimentally obtained curves; the two reported modulated porous-layer coatings, a uniform porous-layer coating, and a plain, polished surface. Table 2 lists the experimental results for the q_{CHF} points of these four curves.

The measurement of the plain surface critical heat flux was $q_{CHF} = 245\ kW/m^2$. The uniform porous-layer coating provided a two fold increase in the critical heat flux, $q_{CHF} = 480\ kW/m^2$, in agreement with results for similar coatings found by other researchers [8–11].

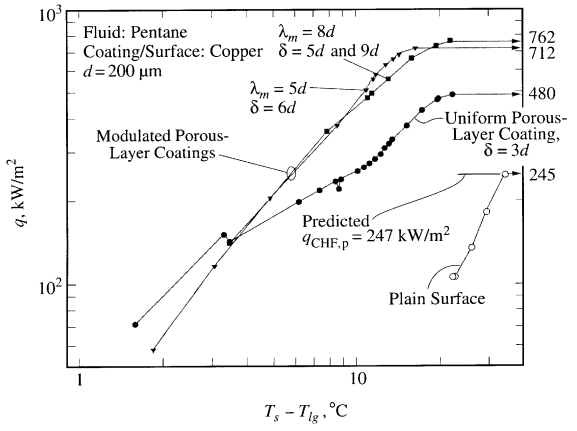

Fig. 15. Measured pool-boiling heat flux from porous-layer coated surfaces.

Table 2
Measured q_{CHF} and the corresponding $T_s - T_{lg}$ for results shown in Fig. 15

	$(T_s - T_{lg})_{CHF}$ (°C)	q_{CHF} (kW/m^2)
Dual height-modulation	22	762
Single-height modulation	16	712
Uniform coating	22	480
Plain surface	34	245

The results for the modulated porous-layer coatings provided an additional fold increase in the q_{CHF} over that of a uniform coating, while further decreasing the surface superheat at high heat fluxes during the nucleate boiling regime. The single-height modulated porous layer coating provided a $q_{CHF} = 711\ kW/m^2$. The dual-height modulated porous layer coating exhibited the greatest enhancement in the q_{CHF} over that of the plain surface, $q_{CHF} = 762\ kW/m^2$, an enhancement of nearly three times. For both modulated porous-layer coatings, the q versus $T_s - T_{lg}$ profiles are nearly equal and are an order of magnitude lower than the plain surface $T_s - T_{lg}$.

5.2. Predicted hydrodynamic liquid-choking limit

The measured $q_{CHF} = 245\ kW/m^2$ for the plain surface was found to be in excellent agreement with that predicted by Eq. (29) as $q_{CHF,p} = 247\ kW/m^2$.

The prediction of the q_{CHF} from the uniform porous-layer coating was made using Eq. (31) with $\epsilon = 0.4$ and $d = 200\ \mu m$. This results in a $\lambda_u = 3.73$ mm, and a predicted $q_{CHF,u} = 478\ kW/m^2$ which agrees very well with the measured value of $q_{CHF} = 480\ kW/m^2$ shown in Fig. 15. The agreement is surprising considering that R_{br} was not measured and an approximation was used. Nevertheless, the excellent agreement between the predicted $q_{CHF,h}$ and the measured q_{CHF} for both the plain and the uniformly coated surfaces lends credence to the hydrodynamic model as a prediction tool for the q_{CHF}.

For the dual-height modulation results shown in Fig. z15, with $q_{CHF} = 762\ kW/m^2$, the corresponding λ_m predicted from Eq. (30) is 1.46 mm, in good agreement with the designed modulation wavelength between the tall center stacks of $\lambda_m = \lambda_b = 8d = 1.6$ mm. Note that the side-to-side distance of the top spherical particles of two adjacent stacks is $\lambda_b - d = 1.4$ mm, and that the predicted λ_m falls between the side-to-side and center-to-center distances.

For the single-height modulation results shown in Fig. 15, with $q_{CHF} = 712\ kW/m^2$, the corresponding λ_m predicted from Eq. (30) is near 1.68 mm, which is greater than the designed $\lambda_b = 5d = 1$ mm. Note though that the next larger length scale across the coating, the distance from one stack to, not one of the six adjacent nearest, but one of the six next nearest stacks is $\lambda_m = (3)^{1/2}\lambda_b = 1.73$ mm, with a side-to-side distance of the top spherical particles of 1.53 mm. Within this theory, this would indicate that a stable wavelength has developed between a pair of nearest, but not adjacent, stacks and extended in between the two adjacent stacks separating them, where the two adjacent stacks do not provide interference destabilizing the interfacial wave.

The measured results for both cases, along with the results for the plain and the uniformly coated surface, are therefore considered to correlate extremely well with that predicted by Eq. (30) and shown in Fig. 13 as a function of a geometric length scale of the coating. It is, however, important to note that the correct length scale for the modulated porous-layer coatings is not always the most obvious one, as shown in the case of the uniform-height stacks. The selection process for the appropriate length scale determining the hydrodynamic liquid-choking limit needs further examination. To determine when side obstacles would create an interference destabilizing a developing interfacial wavelength, the radius of action (magnitude) of the wave must be determined. This is beyond the scope of the current work and is left for future consideration. Note, though, that in the case of the dual-height coating, the presence of the short stacks introducing the interference would explain why the critical heat flux corresponded with the spacing between two nearest tall stacks, instead of the next nearest.

5.3. Predicted wetted-surface regime and viscous-drag liquid-choking limit

The viscous-drag model allowed for the prediction of the wetted-surface regime up to and including the $q_{CHF,v}$. The slope of the predicted q versus $T_s - T_{lg}$ curve for the wetted surface regime is considered to be in fair agreement with the measurements. Both the prediction and measurements are shown in Fig. 17. For a given surface heat flux, the model can be seen to overpredict the $T_g - T_{lg}$, but it is still considered to be in fair agreement with the measurements. At $q_{CHF} = 711$ kW/m^2, measured for the single-height modulation, the measured $T_s - T_{lg} = 16$°C. The model predicts a value of $T_s - T_{lg} = 22$°C, a difference of 38%.

The $q_{CHF,v}$ is dependent on the liquid velocity distribution, the particle size d [through the coating thickness $\delta(d)$, and the permeability, K], the particle and liquid thermal conductivities k_s and k_l, and the porous-layer macrostructure (i.e., the λ_b and the modulation geometry of the cones, etc.). An analytical expression was given in Eq. (24) to approximate the numerical results. The dependence on the included cone angle has been included through the use of an empirical coefficient C_θ that accounts for the diverging flow area through the flow corridor and the corresponding increase in viscous-drag resistance through the artery region. This was found to be nearly independent of d and was shown in Fig. 10. The dependence on particle diameter is shown in Eq. (21) where $\delta = \delta(d)$. Here it was noted that as the diameter of the system decreased, the inertia term (i.e., $We_{K^{1/2}}$) in Eq. (18) became negligible and the solution became Darcy (or viscous) limited. This is shown in Fig. 16, for C_θ $(\theta = 20°) = 0.4$, along with the Darcy

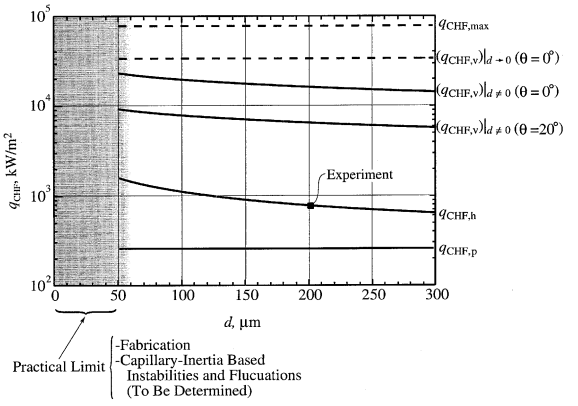

Fig. 16. Variation of the predicted hydrodynamic and viscous-drag liquid-choking limits with respect to d. Also shown is the Darcy limit for the viscous-drag liquid-choking limit, and the experimental result for the dual-height modulated porous-layer coating.

limit and the prediction of $q_{CHF,h}$ from Eq. (30). Variations in these parameters can raise or lower the $q_{CHF,v}$, as well shift the q versus $T_s - T_{lg}$ curve left or right.

The predicted $q_{CHF,v}$ for a particle stack with $d = 200$ μm and $\delta = 6d$ was $q_{CHF,v} = 4760$ kW/m^2. This is higher than both the predicted $q_{CHF,h}$ and the measurements by an order of magnitude. A more realistic flow distribution would be expected to increase the liquid-flow resistance and reduce the predicted viscous-drag liquid-chocking limit, but it is not believed that the $q_{CHF,v}$ would actually fall below the predicted $q_{CHF,h}$ for those coatings.

The formulation of the $q_{CHF,v}$ assumed complete phase separation where the porous stacks were considered to be completely liquid saturated and the vapor flowed only between the stacks. If vapor–liquid counterflow was considered to occur within the stack, the viscous liquid-flow resistance would increase substantially for the same surface heat flux, q. Additionally, the liquid-flow resistance also increases with the porous-layer thickness. Therefore a deep uniform porous-layer, in which there was liquid–vapor counterflow, would be expected to have a high liquid-flow resistance and to exhibit a low counterflow critical heat flux, $q_{CHF} = q_{CHF,cf}$. The expression for $q_{CHF,cf}$ from Udell [17] was given in Eq. (2). For pentane boiling in a deep porous layer consisting of particles of $d = 200$ μm and $\epsilon = 0.4$, this results in a $q_{CHF,cf} = 760$ W/m^2, three orders of magnitude less than for the thin modulated porous-layer coatings.

5.4. Predicted boiling curve of capillary surfaces

Fig. 17 shows the experimental results plotted against the numerical predictions. The predicted $q_{CHF,h}$, from

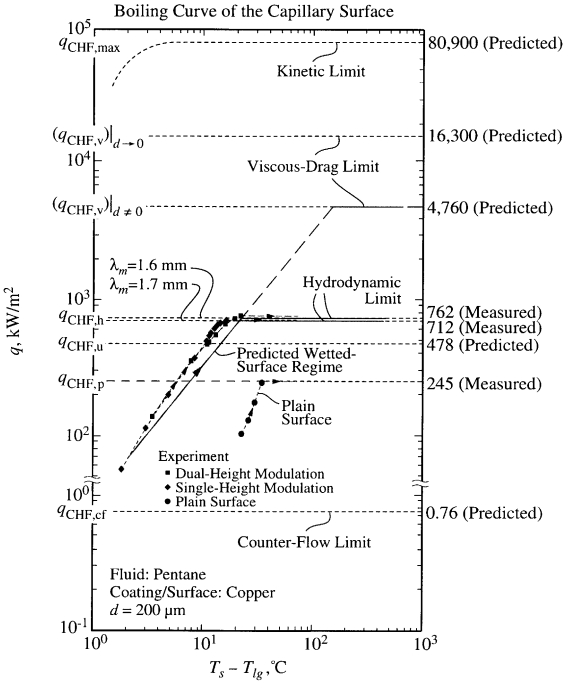

Fig. 17. Comparison of the measured and predicted pool-boiling heat flux from modulated porous-layer coated surfaces.

Eq. (30), for the λ_m suggested by each of the two modulated porous-layer coatings, is shown along with the prediction of the q versus $T_s - T_{lg}$ curve up to the $q_{CHF,v}$ from the viscous-drag numerical model for the uniform-height coating.

By our theory, the surface q versus $T_s - T_{lg}$ would follow the viscous-drag predicted q versus $T_s - T_{lg}$ until either of the two liquid-choking limits occurs. In this case the predicted viscous-drag liquid-choking limit is much higher than the predicted hydrodynamic limit, i.e., $q_{CHF,v} = 4760$ kW/m^2 K $\gg q_{CHF,h} = 762$kW/m^2 K. Therefore this coating is predicted to be hydrodynamically limited and the portion of the predicted q versus $T_s - T_{lg}$ for $q_{CHF,h} < q < q_{CHF,v}$, depicted by the long-dashed line, is not observed. The experimental boiling curve is then predicted to follow the solid lines as shown in Fig. 17.

6. Discussion of optimization

Two types of optimization of modulated porous-layer coatings can be considered, namely, the reduction in $T_s - T_{lg}$ and the increase in q_{CHF}.

The modulated porous-layer coating is an example of an artery-evaporator system as described above. The concept of an artery-evaporator system in itself is only limited by the viscous-drag liquid-flow resistance. It is the macrostructure shape of the system and the locations and means of vapor escape from the system that can further limit the q_{CHF} by introducing hydrodynamic liquid-flow resistance. Optimization of the q_{CHF} can be achieved by minimizing the flow resistance to vapor escape from the surface, i.e., maximizing the liquid-choking limit. In the case of the uniform and modulated porous-layer coatings presented here, the vapor is given to escape by buoyancy into the liquid pool, and thus places the hydrodynamic limit on the liquid supply to the artery.

For hydrodynamically limited surfaces, it is proposed that $q_{CHF} = q_{CHF,h}$ increases with decreasing λ_m down to a theorized liquid-curvature limit $\lambda_{m,min}$, below which the $q_{CHF,h}$ would decrease from the maximum possible value towards the q_{CHF} of a surface with a uniform porous-layer coating. The maximum $q_{CHF,h}$ is a function of the fluid properties and the coating macrostructure, and therefore would indicate the optimum pool boiling q_{CHF} that can be achieved by an opened-modulation porous-layer coating in which the vapor escapes back through the liquid in a buoyant counterflow. The minimum λ_m has not yet been determined or experimentally verified and is left for future consideration. It is possibly related to the decreasing radius of curvature across two modulation peaks as the modulation wavelength is decreased. This would determine a minimum stable bubble departure diameter, dependent on surface tension, for the vapor to escape into the liquid pool. If this bubble diameter is near the λ_m, then there will be increased resistance to the vapor leaving the porous layer from in between stacks creating a vapor accumulation near the surface that would increase the liquid-flow resistance to the incoming liquid supplying the artery.

Since, by comparison with experiment as shown in Fig. 13, our surfaces appear to be hydrodynamically limited, discussion of optimization of the $q_{CHF,v}$ appears to be academic. But if a means of removing the hydrodynamic limitation is achieved, then an artery-evaporator system optimized for the viscous-drag limit could potentially provide an additional order of magnitude increase in the q_{CHF} of an uncoated surface while still maintaining low $T_s - T_{lg}$.

The viscous-drag model does, however, allow for discussion of the enhancement of the $T_s - T_{lg}$. From Eq. (17) the $T_s - T_{lg}$ can be seen to vary with the particle size. There must exist a minimum d below which the enhancement would degrade until at $d \to 0$ the $T_s - T_{lg} = (T_s - T_{lg})_p$. Determination of this minimum optimized d is left for future consideration. There is now a practical limitation on d imposed by fabrication. Within the proposed method of using graphite molds and sintering processes for creating a macrostructured system, it is expected that machining limitations of the mold would prevent the use of particle sizes of less than $d = O(50\ \mu m)$. Currently, the quality of the graphite

used for the molds has limited this study to particles of $d = 200$ μm. Experiments on coatings made with particles of smaller d are left for future considerations.

Optimization of the $T_s - T_{lg}$ can further be achieved by maximizing the rate of evaporation per unit surface area. The evaporation was noted, through predictions from the numerical viscous-drag model, to occur mainly along the sides of the lower portion of the conical particle stacks. The evaporation rate can be increased by maximizing the capillary liquid-pumping and the size of the evaporation zone. The liquid-pumping can be increased by optimizing the balance between the opposing

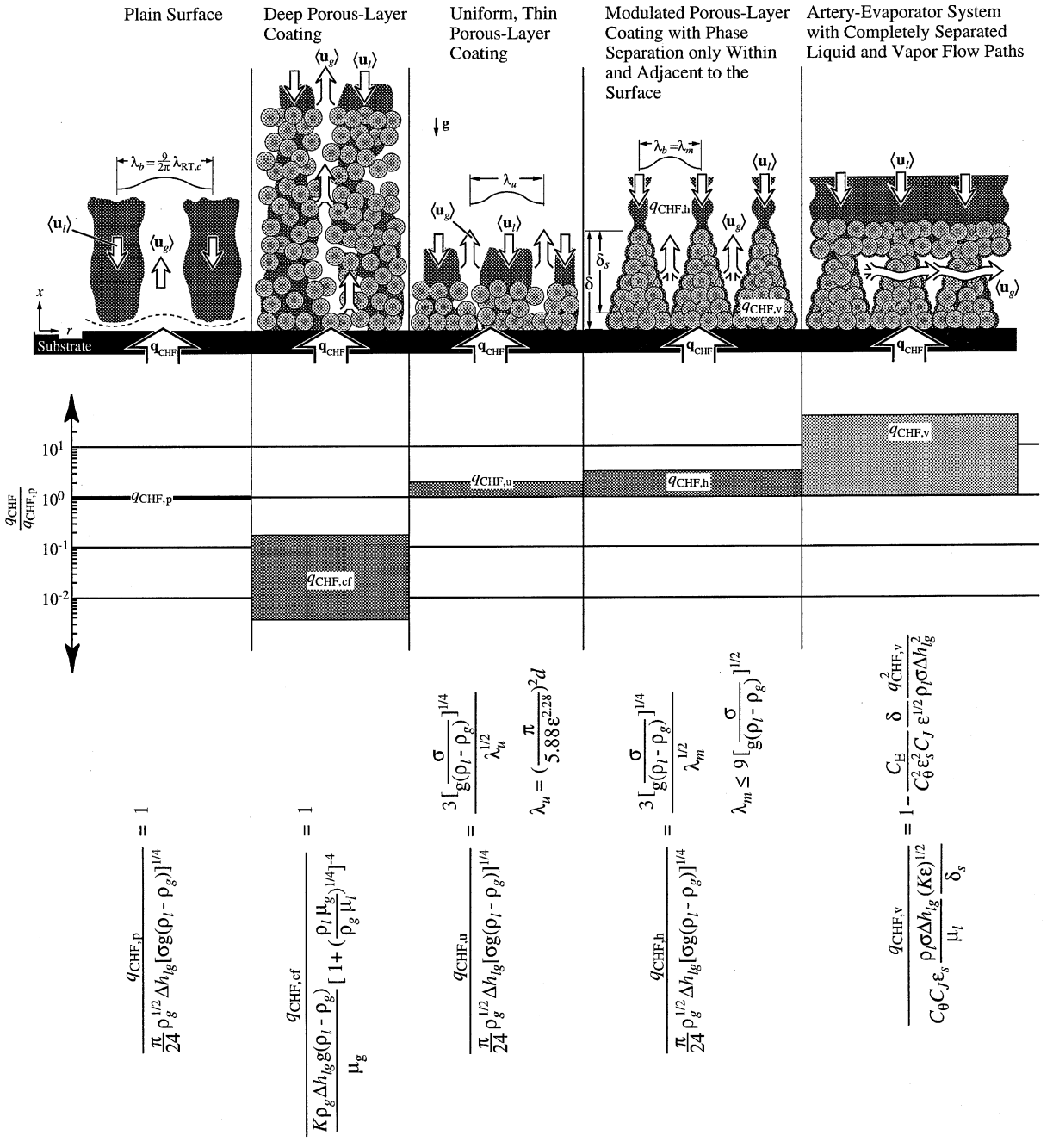

Fig. 18. Comparison of various predicted liquid-choking limits, and a schematic rendering of the surface and/or coating structure and the liquid and vapor flow paths.

capillary and viscous-drag forces, i.e., by decreasing the particle size. The interfacial area of the evaporation zone can be increased either by increasing the number of particle stacks per unit surface area, or by increasing the effective conductivity, $\langle k \rangle$, of the stack to enable the heat flux to conduct further into the artery region in order to utilize more of the side area of a stack. The current fabrication technique does not allow for easy increase of these parameters.

As a proposed (not fabricated) artery-evaporator system that would not be hydrodynamically limited, consider a porous-layer coating with modulation stacks of uniform height on top of which a thin porous layer of uniform thickness (denoted as the cover layer) is sintered. The liquid pool would then be adjacent to the top of the cover layer. This is shown schematically in Fig. 18 in the furthest system on the right and labeled as the artery-evaporator system with completely separated liquid–vapor flow paths. The cover layer in such a system would draw liquid in by capillarity and act as a barrier to vapor flow. The generated vapor would then escape along the path of least flow resistance, in this case, laterally between the modulations, underneath the cover layer, and outwards to the edge of the coated surface. It is assumed that the width of the coated test piece is small enough to render the lateral vapor pressure drop negligible (i.e., no vapor–flow resistance and no high-pressure vapor breakthrough in the cover layer). In this type of design, there is no liquid–vapor counterflow at the liquid entrance into the artery, and therefore the hydrodynamic liquid-choking would not occur, leaving the q_{CHF} of the system to be determined by the liquid-drag viscous-choking limit. Furthermore, in such a design, the vapor is no longer depending on buoyancy to remove it from the liquid entrance into the artery, and therefore the performance would be independent of gravity and orientation as long as the liquid pool was kept in contact with the cover layer. The vapor, once it reaches the side of the coated surface and leaves the porous-layer coating, could then be directed to a condenser to resupply the liquid pool. Such a system, fully utilizing the benefits of complete phase separation could potentially provide a means to realize the order of magnitude enhancement over that of a plain surface as predicted by the viscous drag model.

The proposed artery-evaporator system with completely separated liquid and vapor flow paths conceptually exemplifies how the q_{CHF} can be increased to where it is governed by $q_{\mathrm{CHF,v}}$ by removing the hydrodynamic liquid-choking mechanism. If the viscous-drag liquid flow resistance can be reduced to zero, then the next limiting mechanism would be that described by the kinetic theory in Eq. (1). This is depicted in Fig. 4. It is not possible to bypass the viscous-drag liquid-choking limit, however, with a system using a porous wick for liquid-pumping through an artery, since this type of system must at some point be viscous limited as shown by Eq. (21).

One result that is clear, and is in agreement with both the hydrodynamic and viscous-drag optimizations, is that the q_{CHF} will increase with decreasing d down to some minimum practical value.

7. Conclusion

Modulation of a porous-layer coating was proposed as a means to enhance the q_{CHF} while reducing the $T_{\mathrm{s}} - T_{\mathrm{lg}}$ of boiling from a plain surface.

Experiments were presented showing that porous coatings with modulation (e.g., conical macrostructures), with currently designed size, shape, and distribution, provide a three-time increase in the q_{CHF} and a substantial decrease in the $T_{\mathrm{s}} - T_{\mathrm{lg}}$ from that for an infinite plain surface, as compared to a maximum of 2 to 2.5 times previously reported in the literature for porous-layer coatings of uniform thickness [8–11,13].

The hydrodynamic limit $q_{\mathrm{CHF,h}}$ and the viscous-drag limit $q_{\mathrm{CHF,v}}$, were proposed as two possible liquid-choking limits for artery-evaporator systems and were discussed. The $q_{\mathrm{CHF,h}}$ depends on the fluid properties and is inversely proportional to a flow-critical length scale corresponding to the coating macrostructure geometry. The $q_{\mathrm{CHF,v}}$ occurs when the viscous-drag on the liquid flow within the liquid supply artery (i.e., within the coating) exceeds the available capillary-gravity pumping. The measured q_{CHF} experienced by the coated surface is predicted to occur corresponding to the lower of the two liquid-choking limits for a given surface-coating-fluid system.

The hydrodynamic liquid-choking limit was given in Eq. (30) as

$$\frac{q_{\mathrm{CHF,h}}}{(\pi/24)\rho_{\mathrm{g}}^{1/2}\Delta h_{\mathrm{lg}}\left[\sigma g(\rho_{\mathrm{l}}-\rho_{\mathrm{g}})\right]^{1/4}} = \frac{3\left[\sigma/g(\rho_l-\rho_g)\right]^{1/4}}{\lambda_m^{1/2}},$$

where λ_{m} was a length scale characterizing the vapor escape locations into the liquid pool from the porous-layer coating or surface. For a plain surface, λ_{m} depends on the balance between buoyancy and surface tension, and is then a function of fluid thermophysical properties. For surfaces with porous-layer coatings, λ_{m} is a function of geometrically determined vapor escape paths and is therefore a function of the porous structure.The viscous-drag liquid-choking limit was given in Eq. (24), which can be expressed as

$$\frac{q_{\mathrm{CHF,v}}}{C_\theta \epsilon_{\mathrm{s}} C_J(\rho_{\mathrm{l}}\sigma\Delta h_{\mathrm{lg}}/\mu_{\mathrm{l}})((K\epsilon)^{1/2}/\delta_{\mathrm{s}})} = 1 - \frac{C_{\mathrm{E}}}{C_J}\frac{\delta_{\mathrm{s}}}{C_\theta^2\epsilon_{\mathrm{s}}^2\epsilon^{1/2}}\frac{(q_{\mathrm{CHF,v}})^2}{\rho_{\mathrm{l}}\sigma\Delta h_{\mathrm{lg}}^2}.$$

All of the liquid-choking limits presented in this work are graphically compared and shown with schematic depictions of the system and liquid and vapor flow paths in Fig. 18.

An idealized viscous-drag numerical model was also presented and provides a method for predicting the q versus $T_s - T_{lg}$ curve from a modulated porous-layer coating. Currently, the model underpredicts the q as a function of $T_s - T_{lg}$, but is considered in fair agreement with the experiment results, especially considering the many assumptions that were made. Some simplifying assumptions (e.g., those regarding the liquid-flow paths and the volume-averaging of the porous media) must be revised and/or reconsidered to bring the predictions into better quantitative agreement.

For the surfaces tested in this study, the q_{CHF} is shown to be hydrodynamically limited. Predictions from Eq. (30), relating the critical heat flux with the appropriate modulation wavelength λ_m of the porous-layer coating, are in good agreement with the experimental results, as was shown in Fig. 13.

It is predicted that further enhancement in the q_{CHF} of modulated porous-layer coatings is possible by reducing the modulation wavelength λ_m down to an optimum value. Further experimental and theoretical investigations are required to determine the optimum modulation wavelength $\lambda_m = \lambda_{m,min}$. It is predicted that improved enhancement in the $T_s - T_{lg}$ is possible by reducing the particle size, d, for a given modulation geometry. It is also suggested that an order of magnitude enhancement in the q_{CHF} from an artery-evaporation system would possibly be achieved by controlling the vapor escape paths to remove the limiting hydrodynamic mechanism.

Acknowledgements

The financial support from the National Science Foundation, through grant CTS 99-0896, is greatly appreciated. Special thanks are also extended to K. Pruss of the University of Michigan for his excellent assistance in making the graphite molds.

Appendix A

The discretized energy equations are as follows, where $T = \langle T \rangle = \langle T \rangle^s = \langle T \rangle^l$.

A.1. Conduction zone

Boundary on bottom surface

$$\frac{T_s - T_{i+1,j}}{(R_{x,k})_{0,j}} = q(A_x)_j \quad i = 0, j = 1 \to N - i_b + 1. \tag{A.1}$$

A.2. Base layer nodes

For $i = 1 \to i_b - 1$:

$$\frac{T_{i,j} - T_{i-1,j}}{(R_{x,k})_{i-1,j}} + \frac{T_{i,j} - T_{i+1,j}}{(R_{x,k})_{i,j}} + \frac{T_{i,j} - T_{i,j-1}}{(R_{r,k})_{i,j-1}} + \frac{T_{i,j} - T_{i,j+1}}{(R_{r,k})_{i,j}} = 0,$$
$$j = 2 \to N - i_b, \tag{A.2}$$

$$\frac{T_{i,j} - T_{i-1,j}}{(R_{x,k})_{i-1,j}} + \frac{T_{i,j} - T_{i+1,j}}{(R_{x,k})_{i,j}} + \frac{T_{i,j} - T_{i,j-1}}{(R_{r,k})_{i,j-1}} = 0,$$
$$j = N - i_b + 1, \tag{A.3}$$

A.3. Artery region

Initializing $j_{e,i} = N - i + 1$ and $j_{o,i} = i_s - i + 1$, then

For $i = i_b$:

$$\frac{T_{i,j} - T_{i-1,j}}{(R_{x,k})_{i-1,j}} + \frac{T_{i,j} - T_{i+1,j}}{(R_{x,k})_{i,j}} + \frac{T_{i,j} - T_{i,j-1}}{(R_{r,k})_{i,j-1}} + \frac{T_{i,j} - T_{i,j+1}}{(R_{r,k})_{i,j}} = 0,$$
$$j = 2 \to j_{o,i} - 1, \tag{A.4}$$

$$\frac{T_{i,j} - T_{i-1,j}}{(R_{x,k})_{i-1,j}} + \frac{T_{i,j} - T_{i+1,j}}{(R_{x,ku})_{i,j}} + \frac{T_{i,j} - T_{i,j-1}}{(R_{r,k})_{i,j-1}} + \frac{T_{i,j} - T_{i,j+1}}{(R_{r,ku})_{i,j}} = 0,$$
$$j = j_{o,i}, \tag{A.5}$$

$$\frac{T_{i,j} - T_{i-1,j}}{(R_{x,k})_{i-1,j}} + \frac{T_{i,j} - T_{i+1,j}}{(R_{x,ku})_{i,j}} + \frac{T_{i,j} - T_{i,j-1}}{(R_{r,ku})_{i,j-1}} + \frac{T_{i,j} - T_{i,j+1}}{(R_{r,ku})_{i,j}} = 0,$$
$$j = j_{o,i} + 1 \to j_{e,i} - 1, \tag{A.6}$$

$$\frac{T_{i,j} - T_{i-1,j}}{(R_{x,k})_{i-1,j}} + \frac{T_{i,j} - T_{i,j-1}}{(R_{r,ku})_{i,j-1}} + \frac{T_{i,j} - T_{lg}}{(R_{r,ku})_{i,j_{e,i}}} = 0,$$
$$j = j_{e,i}, \tag{A.7}$$

For $i = i_b + 1 \to i_s - 1$:

$$\frac{T_{i,j} - T_{i-1,j}}{(R_{x,k})_{i-1,j}} + \frac{T_{i,j} - T_{i+1,j}}{(R_{x,k})_{i,j}} + \frac{T_{i,j} - T_{i,j-1}}{(R_{r,k})_{i,j-1}} + \frac{T_{i,j} - T_{i,j+1}}{(R_{r,k})_{i,j}} = 0,$$
$$j = 2 \to j_{o,i} - 1, \tag{A.8}$$

$$\frac{T_{i,j} - T_{i-1,j}}{(R_{x,k})_{i-1,j}} + \frac{T_{i,j} - T_{i+1,j}}{(R_{x,ku})_{i,j}} + \frac{T_{i,j} - T_{i,j-1}}{(R_{r,k})_{i,j-1}} + \frac{T_{i,j} - T_{i,j+1}}{(R_{r,ku})_{i,j}} = 0,$$
$$j = j_{o,i}, \tag{A.9}$$

$$\frac{T_{i,j} - T_{i-1,j}}{(R_{x,ku})_{i-1,j}} + \frac{T_{i,j} - T_{i+1,j}}{(R_{x,ku})_{i,j}} + \frac{T_{i,j} - T_{i,j-1}}{(R_{r,ku})_{i,j-1}} + \frac{T_{i,j} - T_{i,j+1}}{(R_{r,ku})_{i,j}} = 0,$$
$$j = j_{o,i} + 1 \to j_{e,i} - 1, \tag{A.10}$$

$$\frac{T_{i,j} - T_{i-1,j}}{(R_{x,ku})_{i-1,j}} + \frac{T_{i,j} - T_{i,j-1}}{(R_{r,ku})_{i,j-1}} + \frac{T_{i,j} - T_{lg}}{(R_{r,ku})_{i,j_{e,i}}} = 0,$$
$$j = j_{e,i}, \tag{A.11}$$

For $i = i_s$:

$$\frac{T_{i,j} - T_{i-1,j}}{(R_{x,k})_{i-1,j}} + \frac{T_{i,j} - T_{i,j+1}}{(R_{r,ku})_{i,j}} = 0, \quad j = j_{o,i}, \tag{A.12}$$

$$\frac{T_{i,j} - T_{i-1,j}}{(R_{x,ku})_{i-1,j}} + \frac{T_{i,j} - T_{i,j-1}}{(R_{r,ku})_{i,j-1}} + \frac{T_{i,j} - T_{i,j+1}}{(R_{r,ku})_{i,j}} = 0,$$
$$j = j_{o,i} + 1 \to j_{e,i} - 1, \tag{A.13}$$

$$\frac{T_{i,j} - T_{i-1,j}}{(R_{x,ku})_{i-1,j}} + \frac{T_{i,j} - T_{i,j-1}}{(R_{r,ku})_{i,j-1}} + \frac{T_{i,j} - T_{lg}}{(R_{r,ku})_{i,j_{e,i}}} = 0,$$
$$j = j_{e,i}, \tag{A.14}$$

A.4. Center column of nodes

$$\frac{T_{i,1} - T_{i+1,1}}{(R_{x,k})_{i,1}} + \frac{T_{i,1} - T_{i,2}}{(R_{x,k})_{i,1}} = 0,$$
$$j = 1, i = 1 \to i_s - 1, \tag{A.15}$$

where

$$(R_{x,k})_{i,j} = \frac{\Delta x}{\langle k \rangle A_{x\ j}}, \quad (R_{x,k})_{0,j} = \frac{\Delta x/2}{\langle k \rangle A_{x\ j}}, \tag{A.16}$$

$$(R_{x,ku})_{i,j} = \frac{\Delta x}{(\langle k \rangle + \langle k \rangle^d) A_{x\ j}} \frac{\exp((Pe_x)_{i,j}) - 1}{(Pe_x)_{i,j} \exp((Pe_x)_{i,j})}, \tag{A.17}$$

$$(R_{r,k})_{i,j} = \frac{\ln(r_{j+1}/r_j)}{2\pi \langle k \rangle \Delta x},$$
$$(R_{r,k})_{i,j-1} = \frac{\ln(r_j/r_{j-1})}{2\pi \langle k \rangle \Delta x}, (R_{r,k})_{i,1} = \frac{\Delta r}{\langle k \rangle A_{r\ 1}}, \tag{A.18}$$

$$(R_{r,ku})_{i,j} = \frac{\Delta r}{(\langle k \rangle + \langle k \rangle^d) A_{r\ j}} \frac{\exp((Pe_r)_{i,j}) - 1}{(Pe_r)_{i,j} \exp((Pe_r)_{i,j})}, \tag{A.19}$$

and

$$(Pe_x)_{i,j} = \frac{\langle (u_l)_{ij} \rangle \rho_l c_{p,l} \Delta x}{\langle k \rangle}, \quad (Pe_r)_{i,j} = \frac{\langle (v_l)_{ij} \rangle \rho_l c_{p,l} \Delta r}{\langle k \rangle}. \tag{A.20}$$

References

[1] F.P. Incropera, Liquid emersion cooling of electronic components, in: A.E. Bergles (Ed.), in: Heat Transfer in Electronic and Microelectronic Equipment, Hemisphere, New York, NY, 1990, pp. 407–444.

[2] N. Wataru, A.E. Bergles, Cooling electronic equipment: Past, present and future, in: A.E. Bergles (Ed.), in: Heat Transfer in Electronic and Microelectronic Equipment, Hemisphere, New York, NY, 1990, pp. 3–39.

[3] A.E. Berles, The current status of heat transfer enhancement, in: S.-J. Deng et al. (Ed.), Heat Transfer Enhancement and Energy Conversion, Hemisphere, New York, NY, 1990, pp. 11–48.

[4] J.R. Thome, Enhanced Boiling Heat Transfer, Hemisphere, New York, 1990.

[5] R. Webb, Principles of Enhanced Heat Transfer, Wiley, New York, NY, 1993.

[6] N.H. Afgan, L.A. Jovic, S.A. Kovalev, V.A. Lenykov, Boiling heat transfer from surfaces with porous layers, Int. J. Heat Mass Transfer 28 (2) (1985) 415–422.

[7] A.E. Bergles, M.C. Chyu, Characteristics of nucleate pool boiling from porous metallic coatings, ASME J. Heat Transfer 104 (1982) 279–285.

[8] J.Y. Chang, S.M. You, Enhanced boiling heat transfer from micro-porous surfaces: effects of a coating composition and method, Int. J. Heat Mass Transfer 40 (18) (1997) 4449–4460.

[9] S.A. Kovalyo, S.L. Soloviyov, Heat transfer and critical heat fluxes in boiling on a porous surface, Heat Transfer – Sov. Res. 22 (3) (1990) 364–375.

[10] S.M. Lu, R.H. Chang, Pool boiling from a surface with a porous layer, AIChE J. 33 (11) (1987) 1813–1828.

[11] S.P. Malyshenko, Features of heat transfer with boiling on surfaces with porous coatings, Therm. Eng. 38 (2) (1991) 81–88.

[12] Y.V. Polezhaev, S.A. Kovalev, Modelling heat transfer with boiling on porous structures, Therm. Eng. 37 (12) (1990) 617–620.

[13] S.L. Soloviyov, Liquid evaporation heat transfer on a porous surface, Heat Transfer – Sov. Res. 18 (3) (1986) 58–64.

[14] W.R. Gambill, J.H. Lienhard, An upper-bound for critical boiling heat fluxes, ASME J. Heat Transfer 111 (1989) 815–818.

[15] N. Zuber, Hydrodynamic aspects of boiling heat transfer, AECU-4439, Physics and Mathematics, US Atomic Energy Commission, 1959.

[16] M. Kaviany, Principles of Heat Transfer in Porous Media, corrected second edition, Springer, New York, 1999.

[17] K.S. Udell, Heat transfer in porous media considering phase change and capillarity – the heat pipe effect, Int. J. Heat Mass Transfer 28 (2) (1985) 485–495.

[18] S.G. Liter, M. Kaviany, CHF Enhancement by Modulated Porous-Layer Coating, in: Proceedings of ASME 1998 IMECE, HTD vol. 361-1, (1998) 165–173.

[19] S.G. Liter, Pool-boiling enhancement and liquid choking limits within and above a modulated porous-layer coating, Ph.D. dissertation, Department of Mechanical Engineering and Applied Mechanics, University of Michigan, 2000.

[20] J.K. Ferrel, J. Alleavitch, Vaporization heat transfer in capillary wick structures, Chem. Eng. Prog. Symp. Ser. 66 (102) (1970) 82–91.

[21] S. Whitaker, Fundamental Principles of Heat Transfer, Krieger, Malabar, 1983.

[22] M. Kavianay, Principles of Heat Transfer, Wiley, New York, 2001.

[23] C.T. Hsu, P. Chang, K.W. Wong, Modified Zehner–Schlunder models for stagnant thermal conductivity of

porous media, Int. J. Heat Mass Transfer 37 (17) (1994) 2751–2759.
[24] J.H. Lienhard, L.C. Witte, An historical review of the hydrodynamic theory of boiling, Rev. Chem. Eng. 3 (3&4) (1985) 187–280.
[25] J.H. Lienhard, V.K. Dhir, Hydrodynamic prediction of peak pool-boiling heat fluxes from finite bodies, ASME J. Heat Transfer Series C 95 (1973) 152–158.
[26] C.F. Beaton, G.F. Hewitt (Eds.), Physical Property Data for the Design Engineer, Hemisphere, New York, 1989.